ROYAL SOCIETY OF CHEMISTRY

Check for updates

Ultrasound-activatable transition metal complexes to potentiate sonodynamic therapy

Lawrence Cho-Cheung Lee [ID] [a] and Kenneth Kam-Wing Lo [ID] *[ab]

Sonodynamic therapy (SDT) is an emerging non-invasive treatment that utilises low-intensity focused ultrasound to activate sonosensitisers at disease sites, leading to the production of reactive oxygen species (ROS) for therapeutic effects. Leveraging ultrasound as the activation source, SDT offers remarkable advantages, including deep tissue penetration, high spatiotemporal precision and excellent biosafety. The efficacy of SDT largely depends on the performance of the ROS sonosensitisers, making the development of more effective agents crucial for improving clinical outcomes. Recently, there has been growing interest in transition metal complexes as sonosensitisers for SDT due to their remarkable properties such as high ROS generation efficiencies and excellent stability that have been well established in photodynamic therapy. In this review, we summarise recent advances in the development of transition metal complexes as ROS sonosensitisers for SDT in the treatment of cancer, microbial infections and cardiovascular diseases. We highlight key design strategies to enhance sonosensitiser performance and to integrate SDT with other therapeutic modalities to achieve synergistic effects. Furthermore, we discuss current challenges in the clinical translation of transition metal-based sonosensitisers for SDT and explore future prospects for advancing their applications in SDT to improve patient outcomes.
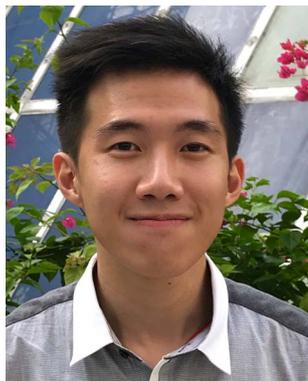
[a]Department of Chemistry, City University of Hong Kong, Tat Chee Avenue, Kowloon, Hong Kong, P. R. China. E-mail: bhkenlo@cityu.edu.hk

[b]State Key Laboratory of Terahertz and Millimetre Waves, City University of Hong Kong, Tat Chee Avenue, Kowloon, Hong Kong, P. R. China

1. Introduction

Traditional drug-based therapies, despite their success, often encounter challenges such as off-target toxicity, drug resistance and limited efficacy in certain pathological conditions. These limitations have spurred the development of innovative

Dr Lawrence Cho-Cheung Lee obtained his BSc and PhD degrees from City University of Hong Kong in 2014 and 2020, respectively. He is currently a Research Fellow under the supervision of Prof. Kenneth Lo. Dr Lee's research is centred on the design of photofunctional transition metal complexes as biological reagents in bioconjugation, bioimaging and (photo)therapeutic applications.

Lawrence Cho-Cheung Lee

Prof. Kenneth Kam-Wing Lo received his BSc and PhD degrees from The University of Hong Kong in 1993 and 1997, respectively. Following his doctoral studies, he was a Croucher Foundation Post-doctoral Research Fellow at the Inorganic Chemistry Laboratory of the University of Oxford. In 1999, he joined the Department of Biology and Chemistry (now the Department of Chemistry) at City University of Hong Kong as an Assistant Professor and was appointed as a Chair Professor in 2023. Prof. Lo's research focuses on the use of luminescent inorganic and organometallic transition metal complexes as biomolecular sensors, imaging reagents and stimuli-responsive photosensitisers for photodynamic therapy.

Kenneth Kam-Wing Lo

therapeutic strategies to improve patient outcomes. One such approach is photodynamic therapy (PDT), a minimally invasive therapeutic modality that uses light to achieve precise spatio-temporal control over therapeutic effects while minimising damage to healthy tissues.[1] Typically, PDT involves the activation of photosensitisers localised at disease sites by light, exciting them from the ground state to the excited states and thereby enabling the conversion of molecular oxygen into reactive oxygen species (ROS) for therapeutic purposes. With rapid advances in light-emitting devices and photosensitisers, PDT has shown significant potential in treating cancer,[2] microbial infections[3] and neurodegenerative disorders.[4] However, the shallow tissue penetration depth of light (<2 cm) renders PDT less effective for targets buried deep within human tissues, limiting its broader clinical applications.[5]

Ultrasound (US) is a mechanical wave with high tissue penetration depth (>10 cm), making it a safe and versatile medical tool for both diagnostic[6] and therapeutic[7] applications. Its non-invasiveness, deep tissue penetration, high spatiotemporal precision, excellent biosafety and low cost have led to the emergence of sonodynamic therapy (SDT), a novel therapeutic modality that utilises low-intensity, focused US (typically 0.5–3.0 W cm^{-2}) to achieve therapeutic effects in deep tissues.[8] Several mechanisms have been proposed to explain the effects of SDT, including ROS generation, cavitation effect and thermal damage (Fig. 1a), with ROS production considered the primary mechanism. In liquid media, US induces the nucleation, growth, oscillation and collapse of microbubbles. The violent collapse of these cavitation bubbles results in a rapid increase in local pressure (81 MPa) and temperature (up to 10 000 K). This process can trigger water pyrolysis, releasing free radicals that react with endogenous substrates to generate ROS and thereby causing oxidative damage to adjacent biomolecules and subcellular organelles. Additionally, US-induced shock waves and thermal effects can trigger mechanical and thermal damage, respectively, to plasma membranes and cellular components, ultimately leading to cell death.

Despite these attractive features, US alone often produces insufficient ROS for significant therapeutic outcomes. The discovery of photoactive hematoporphyrin as a sensitiser for US-induced cytotoxic effects[9] has driven the development of both small molecules[10–12] and nanomaterials[13–15] as sonosensitisers, which enhance ROS production via distinct mechanisms. Small molecule-based sonosensitisers are typically excited by sonoluminescence (i.e., light generated upon bubble collapse), which promotes the population of their excited states for generating ROS such as superoxide anion ($O_2^{\bullet-}$) and hydroxyl ($HO^\bullet$) radicals via electron transfer (type I), or singlet oxygen ($^1O_2$) via energy transfer (type II) (Fig. 1b).[10–12] In contrast, inorganic semiconductor-based nanosonosensitisers produce ROS via US-mediated bandgap excitation, where sonoluminescence or US-induced mechanical stress triggers electron transfer from the valence band (VB) to the conduction band (CB), generating free charge carriers that drive redox reactions with O_2 and H_2O (Fig. 1c).[13–15] First-in-human clinical trials of SDT are ongoing for recurrent high-grade glioma (NCT04559685, NCT04845919, NCT05362409, NCT06039709 and NCT06665724), carotid atherosclerosis (NCT03871725) and peripheral artery disease (NCT03457662), using sinoporphyrin sodium or 5-amino-levulinic acid (5-ALA; a precursor to protoporphyrin IX (PpIX) via the haem biosynthesis pathway) as the ROS sonosensitiser. Unfortunately, these porphyrin derivatives often suffer from poor aqueous solubility, low ROS sensitisation efficiencies and stability under US exposure, as well as suboptimal pharmacokinetics,[16] highlighting the need for more robust alternatives to advance SDT into broader clinical applications.

Over the past few years, there has been rapidly emerging interest in metal-based ROS sonosensitisers for SDT due to their unique properties.[17–19] Of particular interest are photofunctional transition metal complexes, which have been well established as promising phototherapeutic agents.[20–22] The presence of a heavy metal centre, such as rhenium(I), ruthenium(II), iridium(III) and platinum(II), substantially enhances spin–orbit coupling (SOC) and promotes intersystem crossing (ISC), facilitating triplet excited state population upon photo-irradiation for ROS production. Additionally, the high excited-state redox potentials of these complexes allow them to oxidise or reduce crucial endogenous biomolecules such as NAD(P)H, thereby disrupting intracellular redox homeostasis and inducing cell death.[23] These complexes also display high
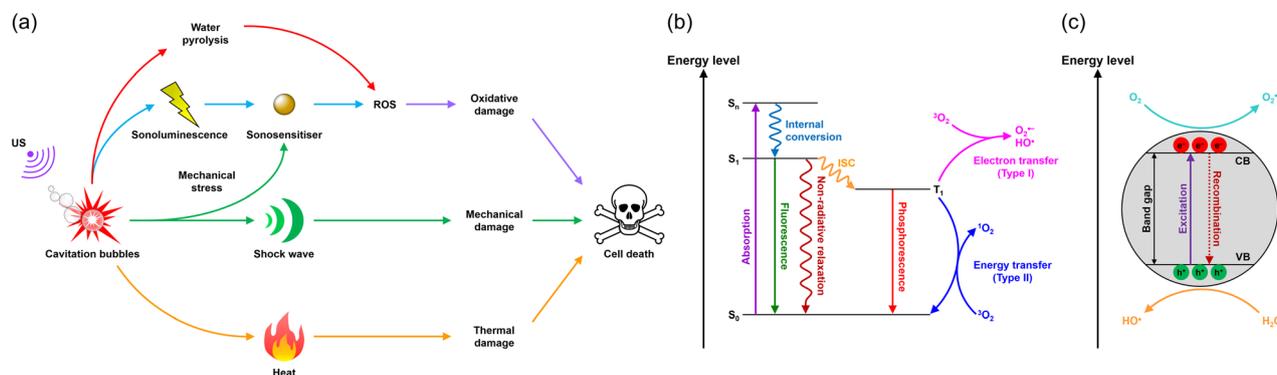

Fig. 1 (a) Schematic illustration of the mechanisms of SDT. (b and c) Simplified diagrams depicting the ROS generation mechanisms of sonosensitisers based on (b) small molecules or (c) inorganic semiconductor nanomaterials.

resistance to photobleaching and photodegradation, which is crucial for achieving phototherapeutic effects at low doses while minimising dark cytotoxicity and other adverse side effects. Furthermore, many transition metal complexes exhibit attractive luminescence behaviour such as environment-sensitive and long-lived emission, which enables real-time monitoring of their cellular uptake and localisation as well as *in vivo* biodistribution, opening up opportunities for luminescence imaging-guided phototherapy.[24–26] Thus, luminescent and photofunctional transition metal complexes have been developed as phototheranostic agents, allowing simultaneous disease diagnosis and treatment in a single platform.[27–29] These remarkable properties have stimulated increasing interest in the development of transition metal complexes as ROS sonosensitisers for SDT.[30]

In this review, we summarise recent advances in the development of transition metal complexes as ROS sonosensitisers for treating cancer, microbial infections and cardiovascular diseases *via* SDT. We focus on molecular design strategies that enhance SDT effectiveness or enable its integration with other therapeutic modalities to achieve synergistic effects. We also discuss current challenges and future prospects for the clinical translation of these complexes. We hope this discussion will inspire further research into transition metal-based SDT agents, broadening their biomedical applications and advancing the clinical use of SDT to improve patient outcomes.

2. Transition metal complexes in sonodynamic therapy for cancer

Cancer remains one of the leading causes of death worldwide, posing a significant global health challenge.[31] Traditional treatments, including surgery, radiotherapy and chemotherapy, are the major treatment of choice in clinical settings. However, these medical interventions suffer from different shortcomings; for example, surgery can trigger the spread of cancer cells from the primary tumour, increasing the risk of metastasis;[32] while radiotherapy and chemotherapy often lead to treatment resistance and poor prognosis.[33,34] Thus, there is an ongoing need for new therapeutic strategies. Owing to its high spatiotemporal precision and minimal invasiveness, PDT has emerged as a prospective alternative, allowing selective tumour eradication with reduced side effects. However, its efficacy is limited by the shallow tissue penetration of light, restricting treatment of deep-seated and less accessible tumours. Leveraging the superior tissue penetration power of US, SDT can overcome this depth barrier, offering new opportunities for effective cancer treatment.

### 2.1. Transition metal complexes for sonodynamic therapy

In 2021, Zhang and co-workers reported the first use of the classical ruthenium(II) complex $[Ru(bpy)_3]^{2+}$ (**1**) (bpy = 2,2′-bipyridine) (Scheme 1) as both a $^1O_2$ sonosensitiser and a sonocatalyst for SDT.[35] Upon sonoexcitation, the complex efficiently sensitises the conversion of O_2 to cytotoxic $^1O_2$ (Fig. 2a and b) and catalyses the oxidation of NADH to NAD^+ (Fig. 2c and d).

This dual action substantially enhances its cytotoxic activity upon exposure to US (3.0 MHz, 0.3 W cm^{-2}, 20 min) (Fig. 2e), with the IC_{50} value decreasing sharply from >20 to 2.91 μM in murine mammary carcinoma 4T1 cells (Table 1). Importantly, owing to the deep tissue penetration of US, the therapeutic effect can reach deep tissues over 10 cm (Fig. 2f), enabling effective inhibition of tumour growth (Fig. 2g–i) and lung metastasis (Fig. 2j) in 4T1 tumour-bearing mice. Ren, Huang, Zhang and co-workers have also developed a water-soluble iridium(III) porphyrin complex (**2**) (Scheme 1) as a dual-function $^1O_2$ sonosensitiser and sonocatalyst for treating deep-seated tumours with SDT.[36] As revealed by laser-scanning confocal microscopy (LSCM), the complex is rapidly taken up by 4T1 cells and specifically enriched in the lysosomes. Upon US irradiation (3.0 MHz, 0.3 W cm^{-2}, 20 min), the complex efficiently generates $^1O_2$ and oxidises endogenous NADH, resulting in high cytotoxicity towards various cancer cell lines ($IC_{50,US}$ = 1.44–7.35 μM; Table 1). *In vivo* experiments demonstrate that the complex induces tumour tissue damage upon US stimulation *via* ROS generation, effectively suppressing tumour growth and metastasis while maintaining high biosafety. These pioneering studies have stimulated the development of transition metal complexes as SDT agents and inspired new design strategies to enhance therapeutic effects.

Lv, Hua, Jiang and co-workers have prepared two iridium(III) thiophenylquinoline complexes (**3**) (Scheme 1) as $^1O_2$ sonosensitisers for SDT.[37] Owing to their long excited-state lifetimes (2.79 and 2.68 μs, respectively), which facilitate interaction with O_2, complexes **3a** and **3b** display *ca.* 1.5- and 1.4-fold higher $^1O_2$ production efficiencies, respectively, than $[Ru(bpy)_3]^{2+}$ upon US triggering. Both complexes are non-cytotoxic in the absence of US ($IC_{50,dark}$ > 20 μM), but exhibit high cytotoxic activity towards 4T1 cells ($IC_{50,US}$ = 9.6 and 9.8 μM, respectively) upon sonoexcitation (1.0 MHz, 1.5 W cm^{-2}, 50% duty cycle, 5 min) (Table 1) *via* the induction of ROS-mediated apoptosis. Zhu, Li, Liu and co-workers have synthesised an iridium(III) 2-(2-pyridyl)benzothiophene complex (**4**) (Scheme 1) as an SDT agent.[38] This complex also possesses a long-lived triplet excited state (τ_T = 2.57 μs) and thus shows more efficient $^1O_2$ sonosensitisation than $[Ru(bpy)_3]^{2+}$. Notably, the complex displays high cytotoxicity towards cancer cells upon US exposure (0.7 W cm^{-2}, 5 min) (Table 1), inducing ferroptosis by downregulating glutathione peroxidase 4 (GPX4) expression and promoting lipid peroxide (LPO) accumulation. *In vivo* studies show that complex **4**-mediated SDT significantly inhibits tumour growth in 4T1 tumour-bearing mice while maintaining favourable biocompatibility.

Guo, Shen, Ru and co-workers have developed a pH-sensitive iridium(III) complex (**5**) (Scheme 1) as an efficient $^1O_2$ sonosensitiser and sonocatalyst for SDT against colorectal cancer.[39] This complex outperforms $[Ru(bpy)_3]^{2+}$ in both sonoinduced $^1O_2$ generation (2.74-fold) and NADH oxidation (2.92-fold). Notably, its sonoactivity is enhanced in acidic environments (pH 4.5), compared to physiological conditions (pH 7.4) due to protonation of the imidazole ring, demonstrating a 22.9- and 7.5-fold increase in $^1O_2$ production and NADH oxidation efficiencies, respectively. After entering murine colorectal
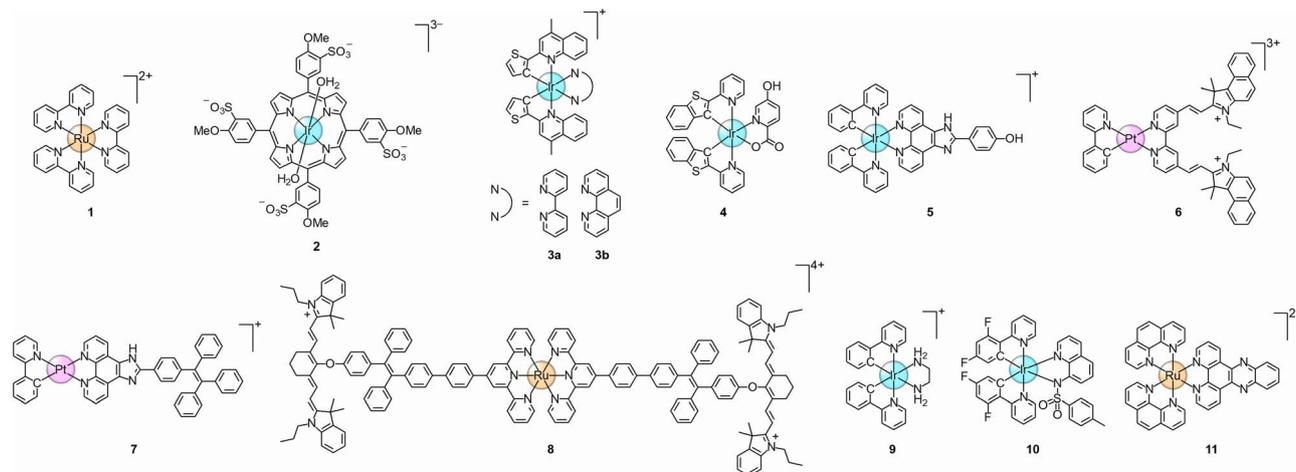
Scheme 1 Structures of complexes **1–11**.

carcinoma CT26 cells, the complex specifically targets the lysosomes and, upon US irradiation, disrupts intracellular redox homeostasis, executing gasdermin E (GSDME)-dependent pyroptosis. The formation of pores in the plasma membrane during pyroptotic cell death facilitates the release of intracellular pro-inflammatory factors such as interleukin-1β, aiding in activating antitumour immune response. Consequently, treatment of CT26 tumour-bearing mice with the complex and US results in a substantial reduction in tumour size.

Zhang and co-workers have designed a cyanine-functionalised platinum(II) complex (**6**) (Scheme 1) for SDT.[40] The incorporation of two cyanine moieties extends the π-conjugation of the diimine ligand, enhancing the absorption and emission of the complex at 400–500 nm and 550–750 nm, respectively. Notably, the complex exhibits more efficient $^1O_2$ generation and thus higher cytotoxic activity towards 4T1 cells when exposed to US (3.0 MHz, 0.3 W cm^{-2}, 20 min; $IC_{50,US} = 6.94$ μM) than under light irradiation (465 nm, 10 mW cm^{-2}, 30 min; $IC_{50,light} = 15.01$ μM), while remaining non-cytotoxic in the absence of US or light ($IC_{50,dark} > 100$ μM) (Table 1). Mechanistic investigations reveal that the sonogenerated $^1O_2$ depletes glutathione (GSH) in cells and downregulates GPX4 expression, which promotes LPO accumulation and thereby induces ferroptosis. Remarkably, the complex induces a more significant reduction in tumour size in 4T1 tumour-bearing mice upon irradiation with US than with light, demonstrating the superior antitumour efficacy of SDT over PDT *in vivo*.

Zhang, Huang and co-workers have developed a tetraphenylethylene (TPE)-modified platinum(II) complex (**7**) (Scheme 1) for SDT.[41] This complex can self-assemble into nanofibers in aqueous media *via* Pt···Pt and π–π interactions, giving rise to intense near-infrared (NIR) emission at 720 nm, which originates from a triplet metal–metal-to-ligand charge-transfer (^{3}MMLCT) state arising from close Pt···Pt contacts. Notably, the assemblies show *ca*. 15.2-fold higher $^1O_2$ sonosensitisation efficiency than the monomer, as the supramolecular self-assembly process substantially enhances ISC efficiency and thereby facilitates $^1O_2$ production. After cellular uptake, the complex primarily localises in the mitochondria and, upon US stimulation (1.0 MHz, 3.0 W cm^{-2}, 10% duty cycle, 20 min), damages the mitochondria and inhibits glucose uptake and aerobic glycolysis, leading to high cytotoxicity towards a range of cancer cell lines ($IC_{50,US} = 2.47$–4.55 μM; Table 1). Importantly, the complex can be activated by US to generate $^1O_2$ in deep tissues at penetration depths greater than 10 cm, effectively suppressing tumour growth in 4T1 tumour-bearing mice.

Lu, Chu, Liu and co-workers have designed a bis-terdentate ruthenium(II) complex (**8**) (Scheme 1) for luminescence imaging-guided SDT.[42] This complex features the incorporation of: (1) π-expansive 2,2′:6′,2″-terpyridine ligands, which facilitate the population of low-lying triplet intraligand (^{3}IL) and intra-ligand charge-transfer (^{3}ILCT) states for ROS generation upon sonoexcitation; (2) the heptamethine cyanine dye IR780, which endows the complex with NIR absorption and emission properties for deep-tissue luminescence imaging; and (3) aggregation-induced emission (AIE)-active TPE units, which allow the complex to maintain strong emission and efficient ROS production in aggregated states. The complex has been encapsulated into an amphiphilic lipid DSPE–PEG$_{2000}$, which consists of 1,2-distearoyl-*sn-glycero*-3-phosphoethanolamine (DSPE) conjugated to polyethylene glycol (PEG), to enhance its aqueous solubility and biocompatibility. As shown by NIR luminescence imaging, the resultant nanoparticles (**PM@8**) display maximum tumour accumulation in human hepatocellular carcinoma HepG2 tumour-bearing mice 24 h post-injection. Subsequent exposure of the tumour region to US significantly inhibits tumour growth, even when the US is applied at the contralateral side of the tumour, highlighting the high penetration power of US in traversing the murine abdominal region to activate the sonosensitiser for treating deep-seated tumours.

Microbubbles are a class of gas-filled microspheres often used in medical imaging[6] and gene or drug delivery.[43] They have also been utilised in SDT to enhance the ROS generation efficiencies and cellular uptake of sonosensitisers.[44] Their nanoscale counterparts, nanobubbles, offer similar advantages while
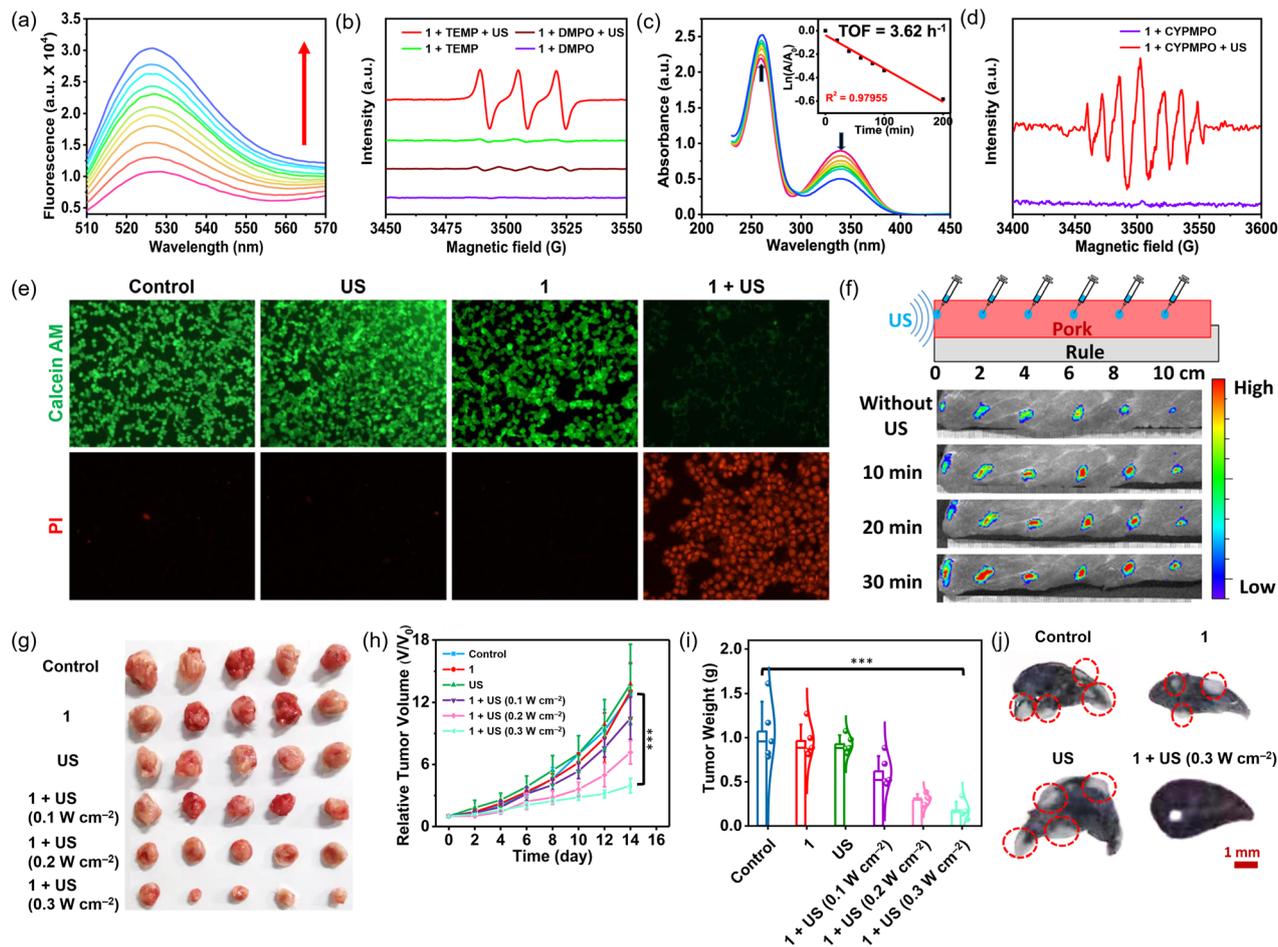
Fig. 2 (a) Time-dependent fluorescence changes of singlet oxygen sensor green (SOSG) (5 μM) in the presence of complex **1** (5 μM) upon US irradiation (3.0 MHz, 0.3 W cm^{-2}) at 10-min intervals for 100 min. (b) Electron paramagnetic resonance (EPR) spectra of complex **1** (4 mM) after US irradiation (3.0 MHz, 0.3 W cm^{-2}, 1 h) using 2,2,6,6-tetramethylpiperidine (TEMP) (8 mM) and 5,5-dimethyl-1-pyrroline N-oxide (DMPO) (18 mM) as spin traps for $^1O_2$ and HO$^•$, respectively. (c) Sonocatalytic oxidation of NADH (150 μM) in the presence of complex **1** (10 μM) upon US irradiation (3.0 MHz, 0.3 W cm^{-2}) for 0, 20, 40, 60, 80, 100 and 200 min. Inset: a plot of ln(A/A_0) at 339 nm against time showing sonocatalytic NADH oxidation turnover frequency (TOF). (d) EPR spectra of complex **1** (5 mM) and NADH (10 mM) after US irradiation (3.0 MHz, 0.3 W cm^{-2}, 1 h) using 5-(2,2-dimethyl-1,3-propoxycyclophosphoryl)-5-methyl-1-pyrroline N-oxide (CYPMPO) (0.02 mg μL^{-1}) as a spin trap for NAD$^•$. (e) LSCM images of 4T1 cells stained with Calcein AM (green) and propidium iodide (PI; red) after various treatments. Complex **1**: 10 μM, 4 h; US: 3.0 MHz, 0.3 W cm^{-2}, 20 min. (f) Luminescence images of pork tissue injected with a mixture of complex **1** (10 μM) and SOSG (10 μM) at 2-cm intervals and subjected to US irradiation (3.0 MHz, 0.3 W cm^{-2}) for 0, 10, 20 and 30 min. (g) Representative photograph of tumours dissected from 4T1 tumour-bearing mice at day 14 after various treatments. (h) Tumour growth curves and (i) average tumour weights of 4T1 tumour-bearing mice after various treatments. ***$p < 0.001$. (j) Horizontal sections of India ink-stained lungs dissected from 4T1 tumour-bearing mice at day 40 after various treatments. Red circles indicate spontaneous pulmonary metastases from the breast tumour. Complex **1**: 0.5 mg kg^{-1}; US: 3.0 MHz, 20 min. Reproduced from ref. 35 with permission from Springer Nature, copyright 2021.

benefiting from improved tumour accumulation through the enhanced permeability and retention (EPR) effect. Strangi, Exner and co-workers have loaded an iridium(III) ethylenediamine complex (**9**) (Scheme 1) into echogenic nanobubbles for enhanced SDT.[45] The complex is incorporated into the shell of lipid shell-stabilised perfluoropropane nanobubbles, affording iridium(III)-modified nanobubbles (**9-NBs**) with an average size of *ca.* 300 nm and a bubble concentration of *ca.* 10^{10} particles per mL across different feeding concentrations of the complex (100, 500 and 1000 μg mL^{-1}). Similar to the free complex, **9-NBs** are efficiently taken up by human breast adenocarcinoma MCF-7 and ovarian adenocarcinoma OVCAR-3

cells and enriched in the cytoplasm. While **9-NBs** are essentially non-cytotoxic, they exhibit potent cytotoxic activity upon US triggering (1.0 MHz, 1.7 W cm^{-2}, 100% duty cycle, 1 min), resulting in more significant cell death than the cells treated with the free complex or a physical mixture of the free complex and nanobubbles due to more effective intracellular ROS production.

Ultrasmall gold nanoparticles (AuNPs), with a diameter less than 10 nm, have demonstrated significant potential in cancer diagnosis and therapy due to their low systemic toxicity, efficient tumour accumulation and fast renal clearance.[46] Zhang and co-workers have conjugated an iridium(III) complex (**10**)

Table 1 Summary of cytotoxic activity and applications of complexes **1–11** and their nanoformulations

Complex/nanoformulation	Cell line	$IC_{50,dark}$	$IC_{50,US}$	Irradiation conditions	Application	Ref.
1	4T1	>20 μM	2.91 μM	3.0 MHz, 0.3 W cm^{-2}, 20 min	SDT	35
2	4T1	>20 μM	3.43 μM	3.0 MHz, 0.3 W cm^{-2}, 20 min	SDT	36
	A549	>20 μM	2.24 μM			
	GL261	>20 μM	7.35 μM			
	HeLa	>20 μM	3.58 μM			
	HepG2	>20 μM	3.70 μM			
	HLF	>20 μM	1.44 μM			
3a	4T1	>20 μM	9.6 μM	1.0 MHz, 1.5 W cm^{-2}, 50% duty cycle, 5 min	SDT	37
3b		>20 μM	9.8 μM			
4	4T1	>50 μM	27.87 μM	0.7 W cm^{-2}, 5 min	SDT	38
	A549	>50 μM	<40 μM			
	HepG2	>50 μM	<40 μM			
	HEK-293T	>50 μM	<40 μM			
5	CT26	—	—	3.0 MHz, 3.0 W cm^{-2}, 10% duty cycle, 20 min	SDT	39
6	4T1	>100 μM	6.94 μM	3.0 MHz, 0.3 W cm^{-2}, 20 min	SDT	40
7	4T1	>50 μM	3.97 μM	1.0 MHz, 3.0 W cm^{-2}, 10% duty cycle, 20 min	SDT	41
	A549	>50 μM	4.15 μM			
	A549R	>50 μM	2.47 μM			
	B16	>50 μM	4.55 μM			
	HepG2	>50 μM	3.15 μM			
PM@8	HepG2	>20 μM	<15 μM	0.5 W cm^{-2}, 5 min	SDT	42
9-NBs	MCF-7	—	—	1.0 MHz, 1.7 W cm^{-2}, 100% duty cycle, 1 min	SDT	45
	OVCAR-3	—	—			
10@BSA-AuNPs	4T1	>10 μM	0.6 μM	3.0 MHz, 0.3 W cm^{-2}, 20 min	SDT	47
PM@TiO$_2$-11	MB49	>28 μg mL^{-1}	<28 μg mL^{-1}	1.0 MHz, 1.2 W cm^{-2}, 40% duty cycle, 1 min	SDT	49
	SV-HUC-1	>28 μg mL^{-1}	>28 μg mL^{-1}			

(Scheme 1) to AuNPs using bovine serum albumin (BSA) as a bridge to yield a nanosonosensitiser (**10@BSA-AuNPs**) for SDT.[47] Upon US stimulation, **10@BSA-AuNPs** generate $^1O_2$ and catalyse NADH oxidation, imparting intracellular redox imbalance to induce cell death. These nanoparticles show efficient uptake in 4T1 cells and primarily localise in the lysosomes, inducing potent cytotoxicity ($IC_{50,US}$ = 0.6 μM; Table 1) upon sonoexcitation (3.0 MHz, 0.3 W cm^{-2}, 20 min). Studies on the mode of cell death indicate that upon US triggering, **10@BSA-AuNPs** induce oncosis, as evidenced by the morphological changes (*e.g.*, cytoplasmic blebbing, nucleus swelling and nuclear chromatin clumping) and upregulation of oncosis-related proteins (*e.g.*, Porimin and Calpain1). Importantly, **10@BSA-AuNPs** efficiently accumulate at the tumour site in 4T1 tumour-bearing mice post-intravenous injection due to the EPR effect. Upon US irradiation, the nanoparticles effectively suppress tumour growth without causing significant toxicity to major organs.

Titanium dioxide (TiO$_2$) nanoparticles are among the most prominent inorganic semiconductors and have been widely explored as photo- and sonosensitisers for PDT and SDT, respectively.[48] However, their ROS production efficiencies remain limited by the wide bandgap and rapid electron–hole recombination. Wang, Chen, Liu and co-workers have developed a narrow-bandgap Schottky heterojunction sonosensitiser (**TiO$_2$-11**) for SDT against bladder cancer.[49] This nanosonosensitiser is constructed by loading a ruthenium(II) dipyrido[3,2-*a*:2′,3′-*c*]phenazine complex (**11**) (Scheme 1) onto TiO$_2$ hollow mesoporous nanospheres. The deposition of the

complex in the TiO$_2$ shell layer facilitates contact between TiO$_2$ and the complex, establishing a Schottky barrier at the interface that reduces the bandgap of TiO$_2$ and promotes electron–hole separation upon US stimulation for boosting ROS generation. To support its biomedical applications, the nanosonosensitiser has been encapsulated into DSPE–PEG$_{2000}$ to improve its dispersibility and hydrophilicity. The resultant nanoparticles (**PM@TiO$_2$-11**) display preferential uptake by bladder carcinoma MB49 cells over normal bladder epithelial SV-HUC-1 cells, with specific enrichment in the lysosomes. Upon US triggering, the nanoparticles induce mitochondrial dysfunction *via* ROS production, inhibiting the migration and proliferation of MB49 cells. Notably, the nanoparticles exhibit longer retention in the bladder in mice bearing an orthotopic MB49 tumour compared to normal mice, with efficient tumour accumulation 1 h post-intravesical instillation. This bladder tumour-specific retention enables substantial tumour suppression upon US exposure with no observable side effects, achieving a survival rate of 100% post-treatment.

2.2. Transition metal complexes for immunogenic sonodynamic therapy

Similar to PDT, SDT can trigger host immune response against cancer cells.[50] However, this antitumour immunity is substantially weakened against solid tumours due to the immunosuppressive tumour microenvironment (TME), which promotes exhaustion and limits infiltration of T cells. To address these challenges, recent research has focused on SDT agents that
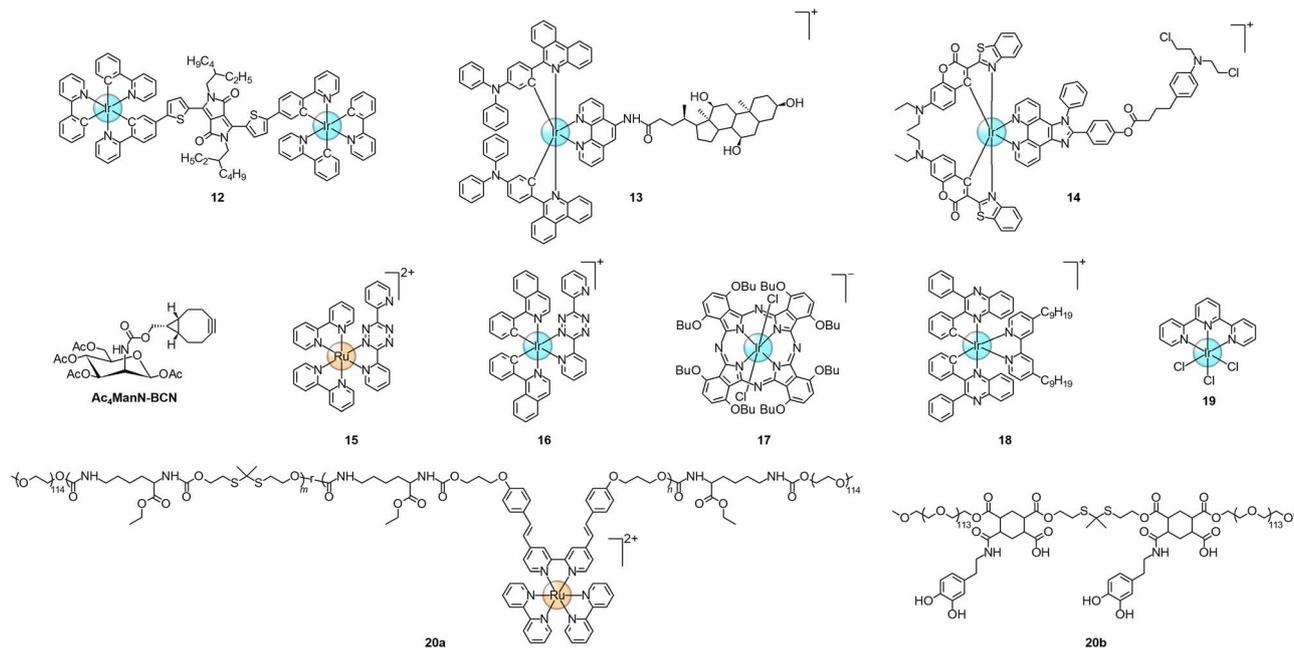
Scheme 2   Structures of complexes **12–20**.

induce immunogenic cell death (ICD).[51–53] During ICD, cancer cells expose calreticulin (CRT) on the cell surface and secrete high mobility group protein B1 (HMGB1) and adenosine triphosphate (ATP) to the extracellular space.[54] These damage-associated molecular patterns (DAMPs) promote dendritic cell (DC) maturation and antigen presentation and thereby enhance the activation, proliferation and tumour infiltration of cytotoxic T lymphocytes (CTLs), eliciting a robust, durable and tumour-specific immune response to inhibit tumour growth, metastasis and relapse. Additionally, the induction of ICD can remodel the immunosuppressive TME and convert immunologically "cold" tumours into "hot" ones, enhancing the effectiveness of immunotherapy.[51–53]

Xiao, Shang and co-workers have prepared a dinuclear iridium(III) complex, where the two iridium(III) moieties are conjugated with an NIR luminescent diketopyrrolopyrrole motif (**12**) (Scheme 2).[55] The complex has been co-assembled with DSPE–PEG$_{2000}$ to increase its water solubility, affording NIR luminescent nanoparticles (**12 NPs**) for imaging-guided SDT. Upon sonoexcitation, **12 NPs** show high efficiency in generating $^1O_2$ and HO$^•$. As a result, **12 NPs** display high cytotoxic activity towards CT26 cells (IC$_{50,US}$ = 14.3 μM; Table 2) upon US irradiation (1.0 MHz, 1.0 W cm^{-2}, 50% duty cycle, 2 min). The nanoparticles also exhibit potent sonocytotoxicity towards human ovarian adenocarcinoma OVCAR-8 cells (IC$_{50,US}$ = 0.5 μM), which remains effective even under hypoxia (IC$_{50,US}$ = 0.7

Table 2   Summary of cytotoxic activity and applications of complexes **12–20** and their nanoformulations

Complex/nanoformulation	Cell line	IC$_{50,dark}$	IC$_{50,US}$	Irradiation conditions	Application	Ref.
12 NPs	CT26	61.3 μM	14.3 μM	1.0 MHz, 1.0 W cm^{-2}, 50% duty cycle, 2 min	SDT	55
		>100 μM^a	56.7 μM^a			
	OVCAR-8	12.8 μM	0.5 μM			
		31.2 μM^a	0.7 μM^a			
HSA@13	4T1	>100 μM	<10 μM	2.0 W cm^{-2}, 50% duty cycle, 5 min	SDT	57
14	4T1	>80 μg mL^{-1}	<40 μg mL^{-1}	1.0 MHz, 1.0 W cm^{-2}, 50% duty cycle	SDT	58
15	4T1	>40 μM	>40 μM	2.0 W cm^{-2}, 50% duty cycle, 5 min	SDT	60
		>40 μM^b	<20 μM^b			
16	4T1	>100 μM	>100 μM	2.0 W cm^{-2}, 50% duty cycle, 5 min	SDT	61
		>100 μM^b	<25 μM^b			
BSA@17	4T1	>100 μM	>100 μM	1.0 MHz, 0.2 W cm^{-2}, 50% duty cycle, 5 min	SDT	64
BiF$_3$@18@PEG	4T1	>80 μg mL^{-1}	16.2 μg mL^{-1}	0.7 W cm^{-2}, 5 min	SDT	65
19-C$_3$N$_5$	A375	>300 μg mL^{-1} ^{a}	—	1.0 MHz, 0.5 W cm^{-2}, 3 min	SDT	66
	B16-F10	>300 μg mL^{-1} ^{a}	—			
20a/20b-Cu^{2+}	MIA PaCa-2	>10 μM	8.7 μM	1.0 MHz, 1.5 W cm^{-2}, 50% duty cycle, 1 min	SDT	69
	Panc 02	>10 μM	<10 μM			

^{a} The cells were cultured under hypoxia. ^{b} The cells were pretreated with **Ac$_4$ManN-BCN** (50 μM, 48 h).

μM) due to efficient HO˙ production. Remarkably, this SDT-mediated ROS burst induces ICD, triggering the release of DAMPs and secretion of inflammatory cytokines. *In vivo* NIR luminescence imaging in a CT26 tumour-bearing mouse model reveals that **12 NPs** show efficient tumour accumulation and retention post-intravenous injection. Subsequent exposure of the tumour site to US substantially suppresses tumour progression, resulting from the effective induction of ICD that promotes the maturation of DCs in the tumour and enhances the infiltration of CTLs to eliminate tumour cells. The **12 NPs**-mediated SDT has been applied in conjunction with cisplatin to treat ovarian cancer in a patient-derived tumour xenograft mouse model. The combined treatment leads to near-complete tumour regression and prolonged survival (up to 60 days), which is significantly longer than with cisplatin alone (36 days), highlighting the synergistic effect of SDT and chemotherapy in cancer treatment.

The endoplasmic reticulum (ER) is a vital organelle involved in protein synthesis, folding and trafficking, as well as lipid and steroid synthesis and calcium homeostasis.[56] Focused ROS generation within the ER can induce ER stress, which activates danger signalling pathways that govern ICD, triggering the release of DAMPs, in particular the surface exposure of CRT that resides in the ER.[54] Pan, Zhao and co-workers have developed an ER-targeting cholic acid-functionalised iridium(III) complex (**13**) (Scheme 2) and loaded it into disulfide-crosslinked human serum albumin (HSA) nanoparticles to give a reduction-sensitive nanosonosensitiser (**HSA@13**) for SDT.[57] This nanoformulation preferentially accumulates at tumour sites, attributed to both the EPR effect and HSA-mediated active targeting. After tumour cell uptake, it disassembles due to reductive cleavage of the disulfide linkages in response to the high levels of intracellular GSH, releasing complex **13** that specifically targets the ER of the cells (Fig. 3a). Upon US stimulation, the localised production of $^1O_2$ and HO˙ in the ER induces severe oxidative damage, intensifying ER stress. This amplifies ICD and triggers the release of abundant DAMPs (Fig. 3b–d), which stimulate the phagocytosis and maturation of DCs (Fig. 3e), facilitate antigen processing and presentation, and thereby promote the activation, proliferation and tumour infiltration of CTLs. The therapeutic efficacy of this ER-targeted SDT has been examined in a bilateral 4T1 tumour-bearing mouse model (Fig. 3f), where US irradiation of the primary tumour substantially inhibits the growth of both primary and distant tumours (Fig. 3g and h). Remarkably, synergising this ER-targeted SDT with immune checkpoint blockade therapy, where an immune checkpoint inhibitor, αPD-L1, is used to block the interaction between programmed death-1 (PD-1) and its ligand PD-L1 to relieve tumour immunosuppression and activate T cells for eradicating tumour cells, elicits more robust adaptive and innate antitumour immune responses, resulting in more significant tumour suppression with complete elimination of distant tumours (Fig. 3g and h). This combined treatment also effectively inhibits lung metastasis, prolonging the survival time of the mice (Fig. 3i and j).

He, Lu, Liu and co-workers have designed a chlorambucil-modified iridium(III) complex (**14**) (Scheme 2) as an ER-targeting $^1O_2$ sonosensitiser for enhanced SDT.[58] After cellular uptake, the complex specifically localises in the ER and efficiently generates $^1O_2$ upon US triggering, inducing ER stress that amplifies ICD and DAMP release, thereby reshaping the immunosuppressive TME. Additionally, the ER stress promotes the proteasomal degradation of hypoxia-inducible factor (HIF)-1α, attenuating the immune evasion of tumour cells. The ER stress also triggers Ca^{2+} flux from the ER to the mitochondria, leading to mitochondrial Ca^{2+} overload, which disrupts mitochondrial membrane potential (MMP) and facilitates the release of mitochondrial DNA into the cytoplasm. This activates the cyclic GMP-AMP synthase–stimulator of interferon genes (cGAS–STING) pathway, inducing the release of interferon-β and repolarisation of M2 macrophages to the M1 phenotype, thereby activating the innate antitumour immunity. Benefiting from the ER stress-mediated multiple modes of action, complex **14** effectively activates both adaptive and innate antitumour immune responses *in vivo* upon sonoexcitation, substantially inhibiting tumour growth without overt organ damage.

Cancer cell membrane has been recognised as a potential therapeutic target due to its unique structure and diverse functions.[59] Extensive membrane damage can enhance the release of DAMPs and boost ICD. Pan, Li, Cai and co-workers have developed a bioorthogonal targeting approach to anchor a ruthenium(II)-based ROS sonosensitiser to the cancer cell membrane for enhanced SDT.[60] This strategy involves two key steps: (1) metabolic glycoengineering of cancer cells to express bicyclo[6.1.0]non-4-yne (BCN) units as artificial receptors on their membrane using a tetraacetylated, BCN-modified mannosamine (**Ac₄ManN-BCN**) (Scheme 2), which is incorporated into cell-surface glycans *via* the native sialic acid biosynthetic pathway; and (2) bioorthogonal labelling of the membrane-bound BCN moieties with a ruthenium(II) tetrazine complex (**15**) (Scheme 2), whose emission and ROS sensitisation capabilities are quenched by the tetrazine unit but restored upon inverse electron-demand Diels–Alder (IEDDA) reaction with BCN derivatives (Fig. 4a and b). The fast reaction rate and high selectivity of the IEDDA reaction between tetrazine and BCN allow precise localisation and activation of the tetrazine complex at the plasma membrane (Fig. 4c). Upon US stimulation, the activated complex produces ROS, causing severe membrane damage and inducing pyroptosis through caspase-1 activation and GSDMD cleavage (Fig. 4d). This is accompanied by significant DAMP release (Fig. 4e–g), which enhances DC maturation and antigen presentation, reshaping the immunosuppressive TME to elicit robust antitumour immune response. To enhance *in vivo* tumour targeting, **Ac₄ManN-BCN** and complex **15** have been encapsulated into GSH- and acid-sensitive HSA nanoparticles, respectively, yielding nanoformulations (**HSA@BCN** and **HSA@15**) that specifically accumulate in tumours and efficiently release their payloads in response to the reductive intracellular and acidic extracellular environments of tumours. The therapeutic efficacy of this hierarchical targeting approach has been examined in bilateral 4T1 or CT26 tumour-bearing mice, where **HSA@BCN** and **HSA@15** are successively administered *via* intravenous injection to enable tumour cell membrane-specific bioorthogonal
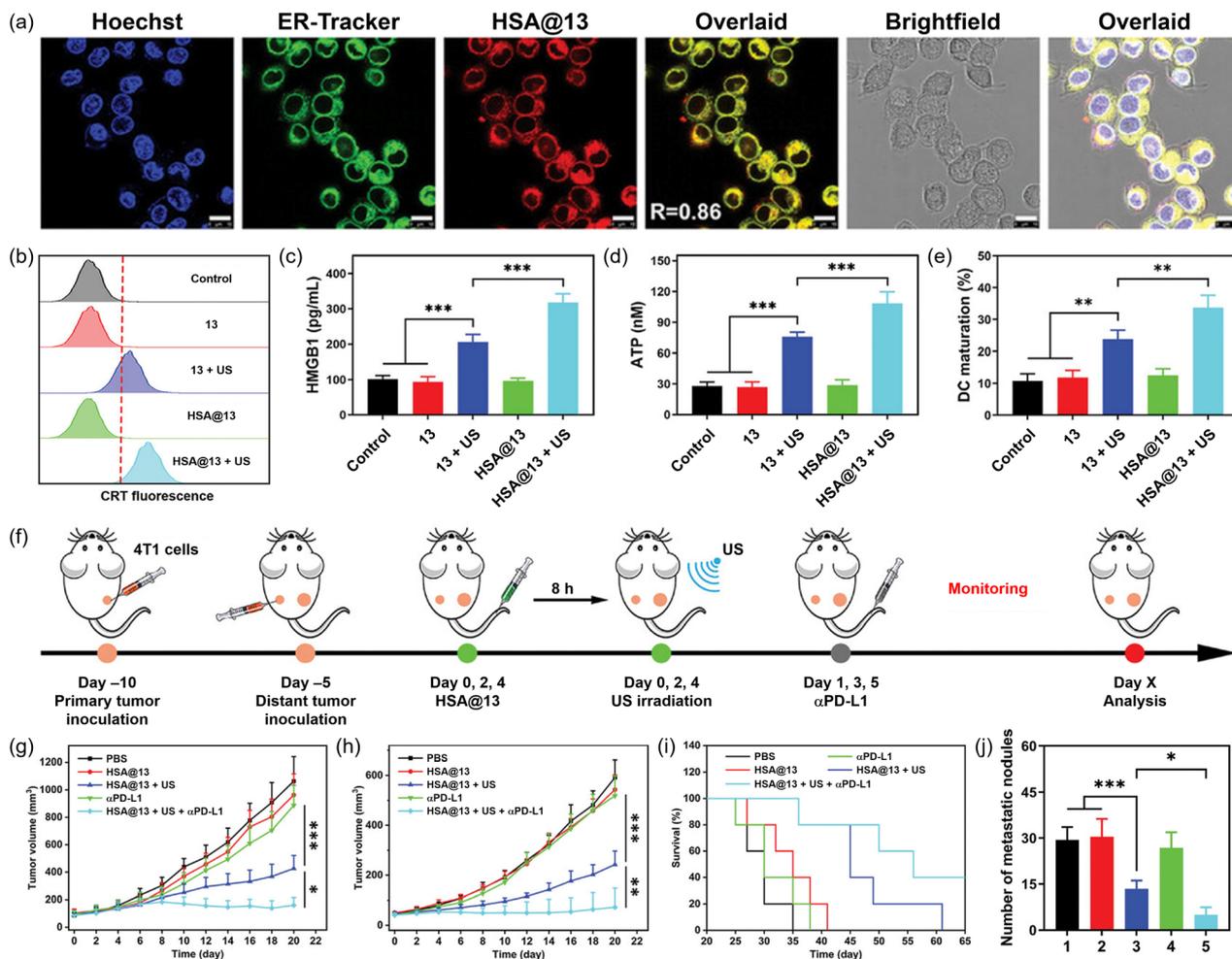
Fig. 3 (a) LSCM images of 4T1 cells incubated with **HSA@13** ([Ir] = 10 μM, 4 h), ER-Tracker Green (30 min) and Hoechst 33342. Scale bar = 10 μm. (b) Flow cytometric analysis of CRT exposure on the surface of 4T1 cells after various treatments. (c and d) Quantification of extracellular (c) HMGB1 and (d) ATP levels in 4T1 cells after various treatments. (e) Quantitative analysis of *in vitro* DC maturation (CD11c$^+$ CD80$^+$ CD86$^+$) induced by pretreated 4T1 cells. Complex **13** or **HSA@13**: [Ir] = 25 μM, 4 h; US: 2.0 W cm^{-2}, 50% duty cycle, 5 min. **$p < 0.01$ and ***$p < 0.001$. (f) Schematic representation of the therapeutic regimen for primary and distant tumours. (g) Primary and (h) distant tumour growth curves of 4T1 tumour-bearing mice after various treatments. (i) Survival rates of 4T1 tumour-bearing mice after various treatments. (j) Quantitative analysis of lung metastatic nodules in 4T1 tumour-bearing mice after various treatments. Group 1: phosphate-buffered saline (PBS); 2: **HSA@13**; 3: **HSA@13** + US; 4: αPD-L1; 5: **HSA@13** + US + αPD-L1. **HSA@13**: 5 mg kg^{-1}; US: 2.0 W cm^{-2}, 50% duty cycle, 5 min; αPD-L1: 100 μg. *$p < 0.05$, **$p < 0.01$ and ***$p < 0.001$. Reproduced from ref. 57 with permission from Wiley-VCH, copyright 2024.

activation of complex **15** (Fig. 4h). Exposure of the primary tumour to US triggers localised ROS generation and activates both adaptive and innate immune responses, effectively inhibiting the growth of primary and distant tumours and suppressing tumour metastasis (Fig. 4i–k). Importantly, the treatment induces durable immune memory, which enables long-term tumour regression even upon tumour rechallenge, substantially increasing the survival time of the mice. A similar targeting approach has also been applied to an iridium(III) tetrazine complex (**16**) (Scheme 2) for effective membrane-targeting SDT, which triggers immunogenic PANoptosis (*i.e.*, a form of cell death that combines the key features of pyroptosis, apoptosis and necroptosis), stimulating antitumour immunity to inhibit tumour growth and metastasis.[61]

Hypoxia is a common characteristic of most solid tumours.[62] The resulting upregulation of HIFs promotes PD-L1 expression in cancer cells, facilitating tumour immune evasion.[63] Du, Liu, Yang and co-workers have assembled an iridium(III) phthalocyanine complex (**17**) (Scheme 2) with BSA to afford a nanoassembly (**BSA@17**) that can alleviate tumour hypoxia for enhanced SDT.[64] In addition to its role as a sonosensitiser for $^1O_2$ production, the nanoassembly can serve as a catalase mimic, catalysing the decomposition of hydrogen peroxide (H_2O_2) to O_2. This suggests that the nanoassembly can convert the high levels of endogenous H_2O_2 in cancer cells into O_2, increasing the O_2 supply for ROS generation during SDT and thereby amplifying the sonocytotoxic effect. Thus, the bifunctional nanoassembly shows high US-mediated cytotoxicity towards 4T1 cells, promoting ICD and the release of DAMPs.
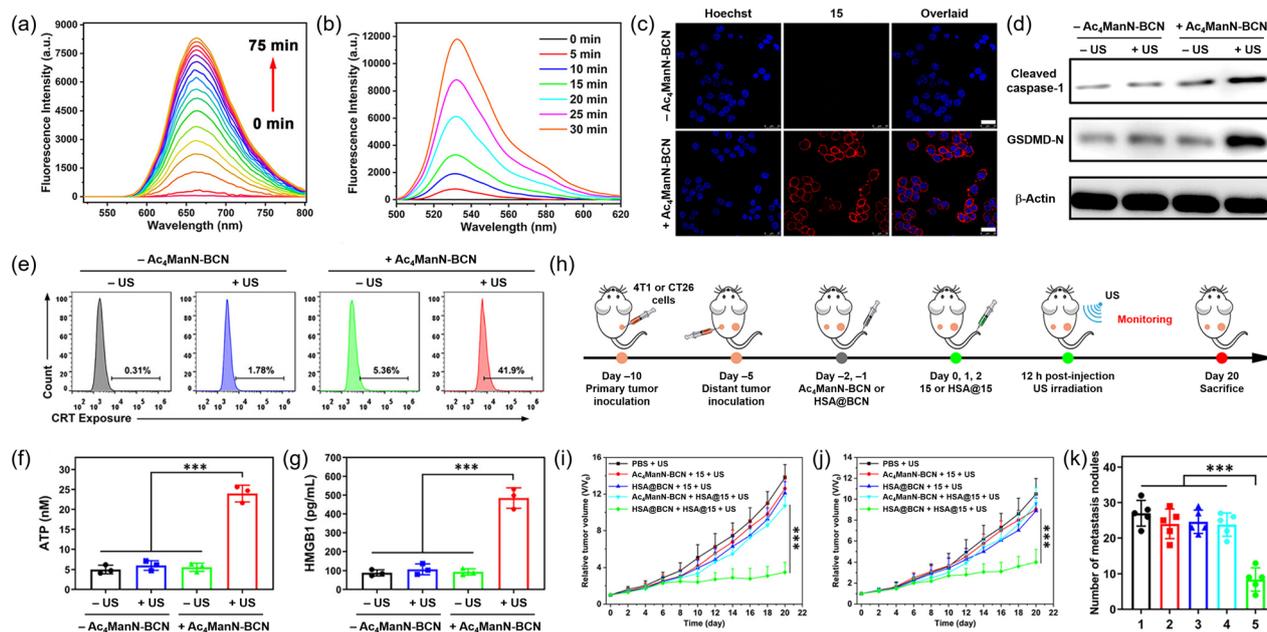
Fig. 4 (a) Time-dependent emission spectra of complex **15** (20 μM) upon incubation with **Ac₄ManN-BCN** (20 μM) at different time intervals for 75 min. (b) Time-dependent fluorescence changes of 2′,7′-dichlorodihydrofluorescein diacetate (DCFH-DA) (5 μM) upon incubation with complex **15** (20 μM) pretreated with **Ac₄ManN-BCN** (20 μM) for 75 min and exposure to US irradiation (1.0 MHz, 2.0 W cm^{-2}, 50% duty cycle) for 0, 5, 10, 15, 20, 25 and 30 min. (c) LSCM images of **Ac₄ManN-BCN** (50 μM, 48 h)-pretreated or untreated 4T1 cells incubated with complex **15** (20 μM, 15 min) and stained with Hoechst 33342. Scale bar = 25 μm. (d) Western blotting analysis of pyroptosis-related protein (cleaved caspase-1 and GSDMD-N) expression in 4T1 cells after various treatments. (e) Flow cytometric analysis of CRT exposure on the surface of 4T1 cells after various treatments. (f and g) Quantification of extracellular (f) ATP and (g) HMGB1 levels in 4T1 cells after various treatments. **Ac₄ManN-BCN**: 50 μM, 48 h; complex **15**: 20 μM, 15 min; US: 2.0 W cm^{-2}, 50% duty cycle, 5 min. (h) Schematic representation of the therapeutic regimen for primary and distant tumours. (i) Primary and (j) distant tumour growth curves of 4T1 tumour-bearing mice after various treatments. (k) Quantitative analysis of lung metastatic nodules in 4T1 tumour-bearing mice after various treatments. Group 1: PBS + US; 2: **Ac₄ManN-BCN** + complex **15** + US; 3: **HSA@BCN** + complex **15** + US; 4: **Ac₄ManN-BCN** + **HSA@15** + US; 5: **HSA@BCN** + **HSA@15** + US. US: 2.0 W cm^{-2}, 50% duty cycle, 5 min; **Ac₄ManN-BCN** or **HSA@BCN**: 40 mg kg^{-1}; complex **15** or **HSA@15**: 5 mg kg^{-1}. ***$p < 0.001$. Reproduced from ref. 60 with permission from the American Chemical Society, copyright 2024.

Additionally, the nanoassembly displays intense NIR absorption, allowing real-time monitoring of its tumour accumulation in 4T1 tumour-bearing mice *via* photoacoustic imaging to guide SDT. Subsequent US irradiation of the tumour site substantially reduces the tumour size. Remarkably, a significant downregulation of HIF-1α and the endothelial marker CD31 in the tumour tissue is observed after the treatment, indicating the successful alleviation of hypoxia and the normalisation of vascular structure, which aid in remodelling the TME for the induction of robust antitumour immune response.

Li and co-workers have loaded an iridium(ɪɪɪ) complex (**18**) (Scheme 2) onto mesoporous bismuth fluoride (BiF₃) nanosheets, which are further modified with PEG, to give an O₂ self-sufficient nanosonosensitiser (**BiF₃@18@PEG**) for SDT.[65] The loading of complex **18** onto BiF₃ nanosheets creates a heterojunction at the interface, which favours charge separation upon US triggering, facilitating electron transfer from BiF₃ to the complex. This promotes the production of ROS from O₂ and H₂O while also catalysing H₂O splitting to evolve O₂, alleviating tumour hypoxia and providing substrates for continuous ROS generation. The substantial ROS production in 4T1 cells induces mitochondrial dysfunction and apoptosis. Notably, the BiF₃ nanosheets undergo rapid degradation in the acidic and

reductive TME, releasing Bi³⁺ that can complex with GSH and thereby disrupt intracellular redox homeostasis. This triggers ROS accumulation and ROS-mediated lipid peroxidation, inducing ferroptosis and ICD to enhance tumour immunogenicity. This SDT-mediated immune activation significantly suppresses primary and distant tumour growth and lung metastasis in bilateral 4T1 tumour-bearing mice.

Zhang, Chao and co-workers have coordinated an iridium(ɪɪɪ) complex (**19**) (Scheme 2) to nitrogen-rich carbon nitride (C₃N₅) nanosheets, yielding an iridium(ɪɪɪ)–C₃N₅ nanocomplex (**19-C₃N₅**) as an O₂ self-sufficient piezo-sonosensitiser for SDT against melanoma.[66] Compared to the unmodified C₃N₅ nanosheets, the nanocomplex exhibits a narrower bandgap and larger dipole moment, which promotes band bending and electron–hole separation, facilitating HO• and O₂•⁻ generation *via* piezoelectric catalysis. Notably, the metal coordination allows the C₃N₅ nanosheets to catalyse the degradation of H₂O₂ to O₂. This self-sustained O₂ production effectively suppresses the expression of HIF-1α and vascular endothelial growth factor-A, reversing the hypoxic TME. Upon cellular uptake by human (A375) and murine melanoma (B16-F10) cells, **19-C₃N₅** specifically localises in the lysosomes and, upon sonoexcitation, triggers lysosomal rupture, evoking pyroptosis *via* autophagy

inhibition. This stimulates the release of DAMPs and activates ICD, reshaping the immunosuppressive TME, promoting macrophage repolarisation as well as T cell activation and infiltration, and ultimately initiating both innate and adaptive immune responses. Thus, **19-C$_3$N$_5$**-mediated SDT effectively inhibits the growth of both primary and distant tumours in bilateral B16-F10 tumour-bearing mice. Remarkably, the treatment elicits durable systemic antitumour immunity, preventing tumour growth, metastasis and relapse. Thus, it significantly suppresses lung metastasis in a mouse model with sentinel lymph nodes, markedly extending the survival rate of the mice.

Copper is an important trace element involved in various physiological processes, and its excessive accumulation triggers cuproptosis, a copper-dependent form of cell death, *via* binding to lipoylated proteins of the tricarboxylic acid (TCA) cycle.[67] Emerging evidence suggests that cuproptosis plays a key role in modulating the TME and thereby regulating antitumour immunity.[68] Xiao, Yang, Jin, Shang and co-workers have designed a US-activatable Cu^{2+}-loaded nanomedicine (**20a/20b-Cu^{2+}**) for inducing cuproptosis to enhance SDT.[69] This nanomedicine is formed upon the self-assembly of two ROS-responsive amphiphilic polymers: a ruthenium(II)-containing polymer (**20a**) and a polyphenol-functionalised polymer (**20b**) (Scheme 2), in the presence of Cu^{2+}. Upon accumulation at the tumour site, US exposure results in the production of ^{1}O$_2$, which cleaves the thioketal linkers in the polymers and triggers nanoparticle degradation, enabling controlled release of Cu^{2+} within cancer cells. The released Cu^{2+} disrupts the TCA cycle, inducing cuproptosis and ICD that activates both adaptive and innate immune responses. Notably, this cuproptosis-targeted

SDT effectively inhibits tumour growth and significantly prolongs survival in various pancreatic tumour mouse models, including subcutaneous, orthotopic and patient-derived xenograft models, highlighting copper homeostasis as a new therapeutic target in cancer therapy.

2.3. Transition metal complexes for combination therapy

While SDT holds strong potential as a non-invasive cancer treatment due to its deep tissue penetration and high spatiotemporal precision, its efficacy is often hampered by its strong dependence on O$_2$ for ROS generation and the high heterogeneity of tumours. Combination therapy, which integrates treatments with distinct mechanisms, has shown significant promise in clinical oncology, offering additive or synergistic therapeutic effects.[70] As a result, growing research efforts focus on combining SDT with other therapeutic modalities to improve cancer treatment.[71–73]

2.3.1. Gas therapy. Gas therapy has emerged as a novel cancer treatment paradigm, leveraging gasotransmitters to induce cancer cell death or modulate the TME.[74] Carbon monoxide (CO), though toxic at high concentrations, exhibits anti-inflammatory and cytoprotective effects at moderate doses, making it a candidate for treating various diseases, including inflammatory disorders, cardiovascular diseases, microbial infections and cancer.[75] Beyond direct inhalation, CO can be delivered *via* CO-releasing molecules (CORMs), which offer precise spatiotemporal control over CO release.[76] Rhenium(I) tricarbonyl complexes have shown great promise as photo-activatable CORMs, releasing CO upon specific light
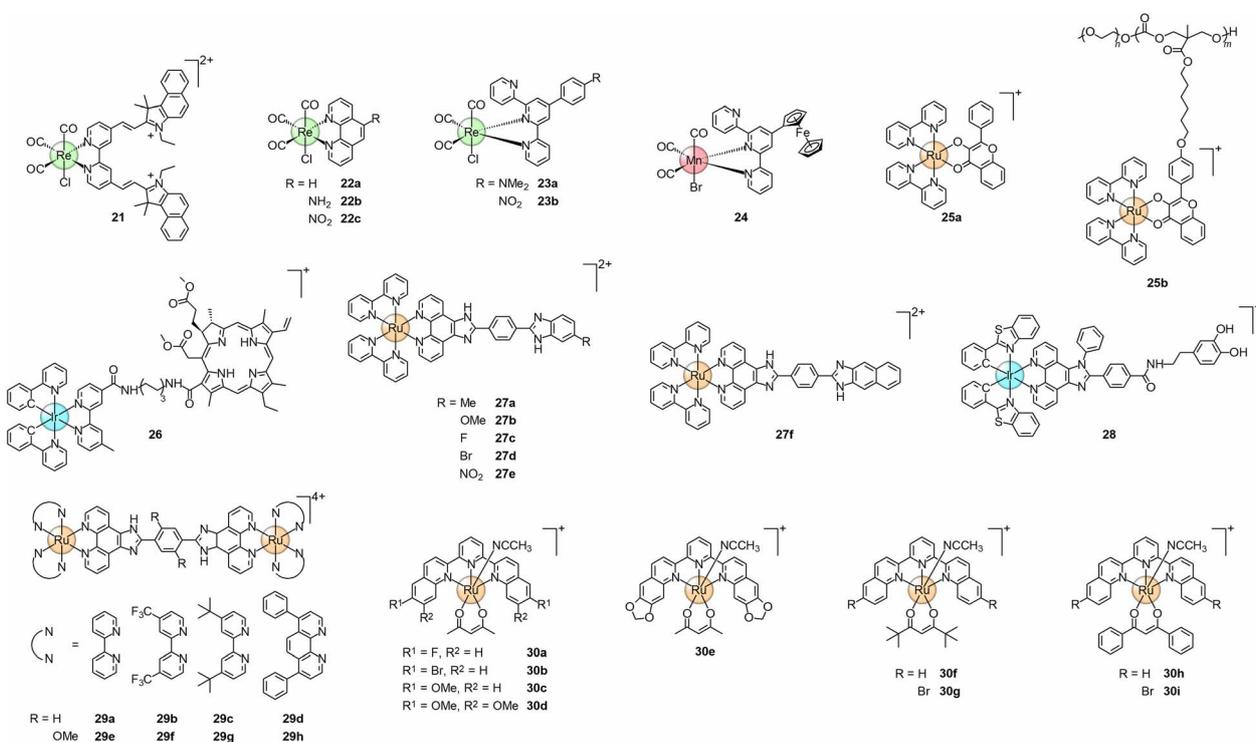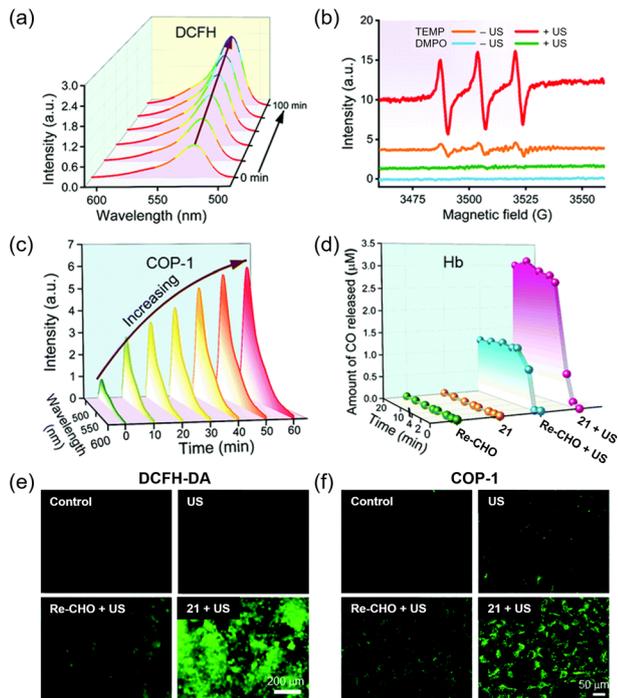

Scheme 3 Structures of complexes **21–30**.

Fig. 5 (a) Time-dependent fluorescence spectra of DCFH–DA (10 μM) in the presence of complex 21 (10 μM) upon US irradiation (3.0 MHz, 0.3 W cm^{-2}) at different time intervals. (b) EPR spectra of complex 21 (4 mM) after US irradiation (3.0 MHz, 0.3 W cm^{-2}, 1 h) using TEMP (8 mM) and DMPO (18 mM) as spin traps for $^1O_2$ and HO$^•$, respectively. (c) Time-dependent fluorescence spectra of CO Probe 1 (COP-1) (10 μM) in the presence of complex 21 (50 μM) upon US irradiation (3.0 MHz, 0.3 W cm^{-2}) for 0, 10, 20, 30, 40, 50 and 60 min. (d) Amount of CO released per micromole of complex 21 or Re-CHO with or without US irradiation, as determined by the haemoglobin assay. (e and f) LSCM images of 4T1 cells stained with (e) DCFH–DA (10 μM, 30 min) or (f) COP-1 (10 μM, 30 min) after various treatments. The cells were incubated with complex 21 or Re-CHO (10 μM, 1 h), washed with PBS, and subjected to US irradiation (3.0 MHz, 0.3 W cm^{-2}, 15 min) prior to staining. Scale bar = (e) 200 or (f) 50 μm. Reproduced from ref. 78 with permission from the Royal Society of Chemistry, copyright 2022.

irradiation.[77] However, their applications as sonoactivatable CORMs (sonoCORMs) remain underexplored.

Banerjee, Zhang and co-workers have designed a cyanine-appended rhenium(ɪ) tricarbonyl complex (21) (Scheme 3) that functions as both a $^1O_2$ sonosensitiser and a sonoCORM for combined SDT and CO gas therapy.[78] The complex shows strong visible-light absorption due to the cyanine moieties that extend the π-conjugation of the diimine ligand. Upon sonoexcitation, the complex displays efficient $^1O_2$ production (Fig. 5a and b) and substantial CO release (Fig. 5c). As determined by the haemoglobin assay, one complex molecule releases three CO ligands upon US stimulation (Fig. 5d). In contrast, the cyanine-free analogue [Re{bpy-(CHO)$_2$}(CO)$_3$(Cl)] (Re-CHO) (bpy-(CHO)$_2$ = 4,4′-dicarboxaldehyde-2,2′-bipyridine) releases only one CO ligand under identical conditions, highlighting the crucial role of the cyanine units in enhancing sonosensitivity. Cellular studies show that complex 21 exhibits preferential uptake by 4T1 cells over normal breast epithelial MCF-10A cells,

demonstrating its intrinsic cancer-targeting capability. As a result, the complex shows potent sonocytotoxic activity towards 4T1 cells (IC$_{50,US}$ = 1.99 μM; Table 3), which is significantly higher than its cyanine-free counterpart (IC$_{50,US}$ = 47.48 μM) due to enhanced $^1O_2$ generation and CO release upon US triggering (3.0 MHz, 0.3 W cm^{-2}, 15 min) (Fig. 5e and f). Mechanistic studies reveal that complex 21 induces ferroptosis via GSH depletion, GPX4 inactivation and LPO accumulation. Remarkably, the complex also displays strong antitumour effect in 4T1 tumour-bearing mice upon US activation, highlighting the synergistic benefits of SDT and CO gas therapy in cancer treatment.

Sadhukhan, Koch, Banerjee and co-workers have evaluated rhenium(ɪ) tricarbonyl complexes with various substituents (22) (Scheme 3) for treating cancer via SDT or PDT.[79] Among these complexes, complex 22b, bearing an electron-donating amino group, exhibits an additional absorption band at ca. 445 nm, enabling efficient $^1O_2$ and HO$^•$ production upon excitation with US (1.5 W cm^{-2}) or visible light (400–700 nm, 5 J cm^{-2}). Its high excited-state reduction potential ($E°$[Re$^{*/-}$] = +0.83 V versus SCE) also allows it to efficiently catalyse NADH oxidation, further disrupting intracellular redox homeostasis. Notably, complex 22b shows efficient CO release upon exposure to US or visible light, in contrast to the unsubstituted or nitro-substituted analogues 22a and 22c that release CO only under UV light irradiation. The dual modes of action of complex 22b underlies its high sono- and photoinduced cytotoxicity towards human cervical adenocarcinoma HeLa cells (IC$_{50,US}$ = 5.01 μM and IC$_{50,light}$ = 1.9 μM; Table 3). Although complex 22b displays relatively higher cytotoxic activity upon irradiation with visible light than US, the superior tissue penetration depth of US suggests that SDT could effectively treat deep-seated tumours.

Lu, Zhang and co-workers have developed two rhenium(ɪ) tricarbonyl complexes (23) (Scheme 3) for treating hypoxic tumours via combined SDT and CO gas therapy.[80] Compared to the nitro-substituted complex 23b, the dimethylamine-modified complex 23a exhibits stronger absorption at ca. 426 nm and emission at ca. 612 nm in aqueous solutions. Upon US stimulation (1.0 MHz, 0.3 W cm^{-2}), both complexes release one CO ligand with comparable efficiencies. However, complex 23a generates $^1O_2$ more effectively than complex 23b. As a result, complex 23a shows higher sonocytotoxic activity towards 4T1 cells (IC$_{50,US}$ = 5.34 μM) compared to complex 23b (IC$_{50,US}$ = 15.44 μM) (Table 3). Importantly, complex 23a retains its activity under hypoxic conditions (IC$_{50,US}$ = 13.24 μM), underscoring the therapeutic benefit of CO gas therapy in treating hypoxic tumours where O$_2$ deficiency limits ROS generation. Additionally, it displays negligible cytotoxic activity towards normal murine fibroblast L929 cells (IC$_{50}$ > 50 μM) with or without US irradiation. The cancer-selective sonocytotoxicity of the complex enables effective tumour inhibition in 4T1 tumour-bearing mice upon US stimulation without side effects.

Koch, Banerjee and co-workers have developed a ferrocene-functionalised manganese(ɪ) tricarbonyl complex (24) (Scheme 3) as both an ROS sonosensitiser and a sonoCORM for combined SDT and CO gas therapy.[81] The ferrocene moiety not only enhances the cellular uptake of the complex due to

Table 3 Summary of cytotoxic activity and applications of complexes **21–25**

Complex	Cell line	$IC_{50,dark}$	$IC_{50,US}$	Irradiation conditions	Application	Ref.
21	4T1	>50 μM	1.99 μM	3.0 MHz, 0.3 W cm^{-2}, 15 min	SDT + CO gas therapy	78
	MCF-10A	>50 μM	>50 μM			
22b	HeLa	>50 μM	5.01 μM	1.5 W cm^{-2}, 10 min	SDT + CO gas therapy	79
23a	4T1	>50 μM	5.34 μM	1.0 MHz, 0.3 W cm^{-2}, 20 min	SDT + CO gas therapy	80
		>50 μM^a	13.24 μM^a			
	L929	>50 μM	>50 μM			
23b	4T1	>50 μM	15.44 μM			
		>50 μM^a	20.69 μM^a			
24	DL	7.3 μM	0.54 μM	1.0 MHz, 0.3 W cm^{-2}, 15 min	SDT + CO gas therapy	81
	MCF-7	13.8 μM	0.87 μM			
	Normal spleen cells	21.8 μM	19.2 μM			
	HEK-293	>10 μM	<10 μM			
25b	4T1	>160 μg mL^{-1}	<10 μg mL^{-1}	1.0 MHz, 1.5 W cm^{-2}, 50% duty cycle, 5 min	SDT + SACT	86
	MCF-7	>160 μg mL^{-1}	<20 μg mL^{-1}			

^{a} The cells were cultured under hypoxia.

increased lipophilicity, but also lowers the S_0–S_1 and S_0–T_1 energy gaps of the complex to 1.45 and 1.43 eV, respectively, facilitating ROS generation upon US triggering. Thus, while the CO release efficiency of complex **24** remains comparable to its ferrocene-free counterpart, it exhibits more efficient $^1O_2$ and HO$^{\bullet}$ production upon sonoactivation. As a result, the complex shows significantly higher sonocytotoxic activity towards Dalton's lymphoma (DL) and MCF-7 cells ($IC_{50,US}$ = 0.54 and 0.87 μM, respectively; Table 3) than the ferrocene-free analogue ($IC_{50,US}$ = 6.24 and 4.18 μM, respectively), inducing cancer cell apoptosis via mitochondrial depolarisation and caspase-3 activation. Notably, the complex displays substantially lower cytotoxicity towards normal spleen and kidney cells even under US exposure ($IC_{50,US}$ = 19.2 and <10 μM, respectively), highlighting its promise for effective cancer therapy in vivo.

2.3.2. Sonoactivated chemotherapy. Sonoactivated chemotherapy (SACT) is a therapeutic approach that utilises US to activate chemotherapeutic prodrugs at targeted tumour sites, offering localised, controlled treatment with reduced systemic toxicity. Several US-activatable platinum(IV) prodrugs have been developed that release active platinum(II) species upon sono-sensitised electron transfer, enabling effective treatment of deep-seated or large tumours.[82–85]

Sun and co-workers have designed a sonoactivatable ruthenium(II) complex (**25a**) (Scheme 3) for combined SDT and SACT.[86] Compared to [Ru(bpy)$_3$]$^{2+}$, the coordination with an electron-rich 3-hydroxyflavone (3-HF) ligand reduces the highest occupied molecular orbital (HOMO)–lowest unoccupied molecular orbital (LUMO) energy gap to 2.70 eV (Fig. 6a), allowing efficient activation via water sonoluminescence. The S_0–T_1 energy gap is also lowered to 0.89 eV (Fig. 6b), falling below the threshold for $^1O_2$ production (0.98 eV), favouring exclusive generation of $O_2^{\bullet-}$ upon US stimulation. Notably, the resultant $O_2^{\bullet-}$ can not only be further converted into highly cytotoxic HO$^{\bullet}$ through the Fenton and Haber–Weiss reaction, but also induce fragmentation of the 3-HF ligand to yield a highly cytotoxic ruthenium(II) benzoate complex (**Ru-BA**) (Fig. 6c). Incorporation of complex **25a** into an amphiphilic

block copolymer affords a metallopolymer (**25b**) (Scheme 3), which forms self-assembled nanoparticles that facilitate tumour accumulation and retention via the EPR effect. After cellular uptake, the nanoparticles specifically target the mitochondria (Fig. 6d) and, upon US exposure, produce ROS and **Ru-BA**. The excessive ROS generation depletes intracellular GSH, downregulates GPX4 and causes LPO accumulation (Fig. 6e–g), inducing ferroptosis. Meanwhile, the released **Ru-BA** binds to mitochondrial DNA (Fig. 6h), leading to mitochondrial dysfunction and apoptosis. Since the nanoparticles can be activated by US at tissue depths of up to a centimetre, they achieve near-complete breast tumour regression in an ortho-topic MCF-7 tumour mouse model and prevent lung metastasis via the suppression of metastasis-related protein expression (Fig. 6i–l).

2.3.3. Photodynamic therapy. Compared to PDT, SDT offers deeper tissue penetration, making it a promising approach for cancer treatment. However, PDT generally produces more ROS due to the direct excitation of photosensitisers. Since many ROS sonosensitisers used in SDT are also photoactive and compatible with both therapies, combining SDT and PDT can boost ROS generation while reducing the required sensitiser dose, resulting in a synergistic therapeutic outcome with fewer side effects.[87]

Zhao, Chao and co-workers have developed an iridium(III) complex conjugated with chlorin e6 (Ce6) (**26**) (Scheme 3) as a dual-modal SDT and PDT agent for treating melanoma.[88] The conjugate sensitises the production of $^1O_2$ upon sono- and/or photoexcitation, exhibiting enhanced $^1O_2$ generation compared to its individual components, [Ir(ppy)$_2$(bpy)]$^+$ (**Ir**) (Hppy = 2-phenylpyridine) and Ce6 (Fig. 7a), indicating a synergy between the iridium(III) complex and Ce6. Additionally, the conjugate shows strong two-photon absorption (Fig. 7b), which allows a higher penetration depth under two-photon excitation with NIR light. The conjugate has been encapsulated into DSPE–PEG$_{2000}$ bearing a terminal biotin group to give nanoparticles (**PM-B@26**) that target biotin receptor-overexpressing cancer cells. The nanoparticles enter
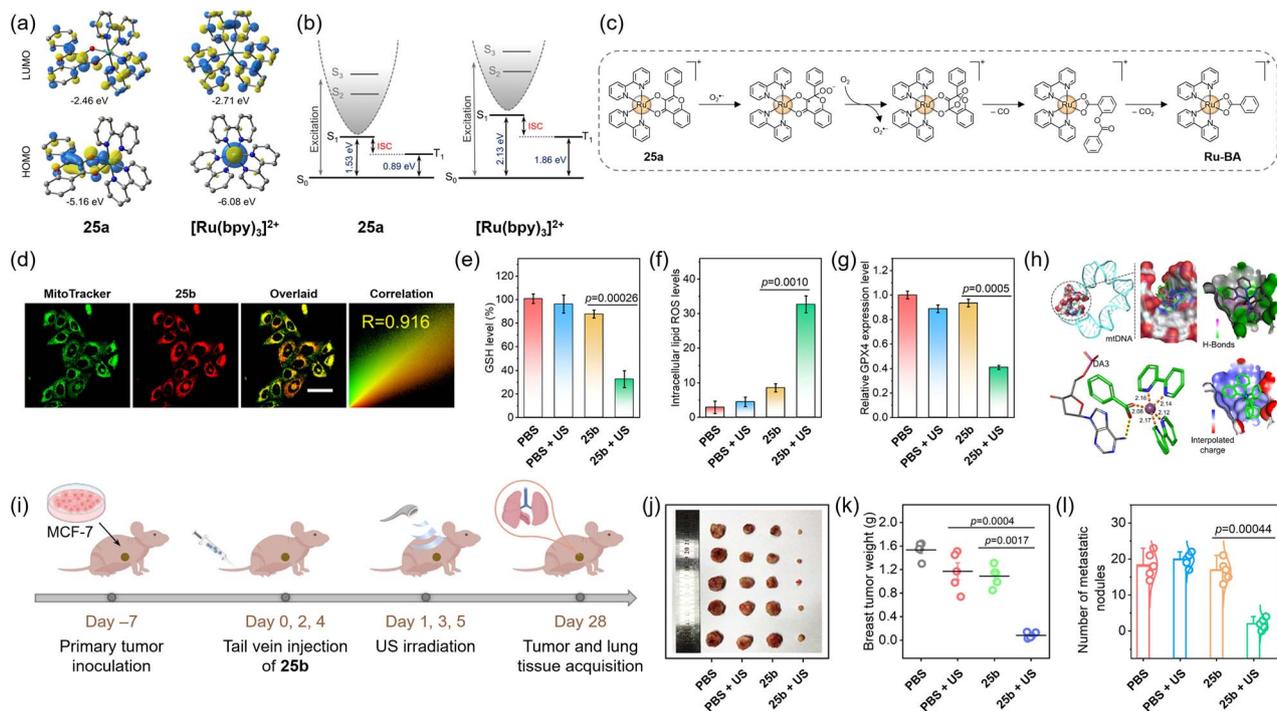
Fig. 6 (a) Frontier orbital distribution of HOMO and LUMO energy levels of complex **25a** (left) and $[Ru(bpy)_3]^{2+}$ (right), calculated at the B3LYP/def2svp/PCM level. (b) Energy profiles of S_1 and T_1 states for complex **25a** (left) and $[Ru(bpy)_3]^{2+}$ (right). (c) The proposed reaction mechanism of complex **25a** with $O_2^{\bullet-}$ under US irradiation. (d) LSCM images of 4T1 cells incubated with complex **25b** (25 µg mL^{-1}) and then MitoTracker Green. Scale bar = 50 µm. (e–g) Intracellular (e) GSH, (f) LPO and (g) GPX4 expression levels in 4T1 cells incubated with complex **25b** (50 µg mL^{-1}, 6 h) with or without US irradiation (1.0 MHz, 1.5 W cm^{-2}, 50% duty cycle, 5 min). (h) Molecular docking calculation of mitochondrial DNA (4nnu) with complex **Ru-BA**. (i) Schematic representation of the therapeutic regimen for primary breast tumours and pulmonary metastases. (j) Representative photograph and (k) average weights of breast tumours dissected from orthotopic MCF-7 tumour-bearing mice after various treatments. (l) The number of metastatic nodules per lung in MCF-7 tumour-bearing mice after various treatments. US: 1.0 MHz, 1.5 W cm^{-2}, 50% duty cycle, 6 min; complex **25b**: 15 mg kg^{-1}. Reproduced from ref. 86 with permission from the American Chemical Society, copyright 2024.

A375 cells *via* endocytosis and primarily localise in the acidic lysosomes, gradually releasing the conjugate that specifically targets the mitochondria (Fig. 7c) due to its cationic and lipophilic character. Upon dual sono- (1.0 MHz, 1.5 W cm^{-2}, 50% duty cycle, 2 min) and photoirradiation (405 nm, 0.5 J cm^{-2}), the conjugate induces MMP reduction and caspase 3/7-mediated apoptosis. Thus, the cytotoxic activity of the nanoparticles is substantially enhanced, with the IC$_{50}$ value decreasing sharply from >12 to 0.40 µM (Table 4), which is an order of magnitude smaller than that observed upon exposure to US (2.64 µM) or light alone (2.08 µM). In contrast, the nanoparticles display negligible cytotoxicity towards human normal liver LO2 cells in the dark or upon combined treatment (IC$_{50}$ > 12 µM) due to their low cellular uptake. Importantly, the nanoparticles efficiently accumulate at the tumour site in A375 tumour-bearing mice post-intravenous injection (Fig. 7d) due to both the EPR and active targeting effects, and effectively suppress tumour growth upon irradiation with both US and NIR light (Fig. 7e–g), enabling near-complete tumour ablation within a single treatment.

Yang, Gao and co-workers have prepared a series of ruthenium(II) complexes (**27**) (Scheme 3) as single-molecule dual-modal agents for combined SDT and PDT against cisplatin-resistant non-small cell lung cancer (NSCLC).[89] The lowest triplet excited states of these complexes are predominantly ^{3}IL in nature, with long lifetimes enabling effective interaction with O_2. Thus, all the complexes efficiently produce ROS upon excitation with US or light, with the bromobenzene- and naphthalene-substituted complexes **27d** and **27f** exhibiting the highest $O_2^{\bullet-}$ and $^1O_2$ generation quantum yields, respectively. Remarkably, the complexes show high cytotoxic activity towards cisplatin-resistant human lung adenocarcinoma A549R cells (IC$_{50,US+light}$ = 0.118–4.57 µM; Table 4) upon exposure to both US (1.0 MHz, 1.0 W cm^{-2}, 50% duty cycle) and NIR light (808 nm, 100 mW cm^{-2}, 30.0 J cm^{-2}). This combined treatment is more effective than SDT (IC$_{50,US}$ = 1.03–67.3 µM) or PDT alone (IC$_{50,light}$ = 0.607–8.76 µM), demonstrating a synergistic effect between the two therapies. Notably, complexes **27d** and **27f** display the most potent activity, with IC$_{50,US+light}$ values of 0.249 and 0.118 µM, respectively. Importantly, their efficacy persists under hypoxic conditions due to dual US- and light-induced ROS generation. Mechanistic studies suggest that complexes **27d** and **27f** predominantly localise in the mitochondria and induce both apoptosis and ferroptosis upon US and NIR light irradiation.

2.3.4. Photothermal therapy. Photothermal therapy (PTT) is an emerging therapeutic approach that utilises photothermal transduction agents to convert light into heat, inducing cell
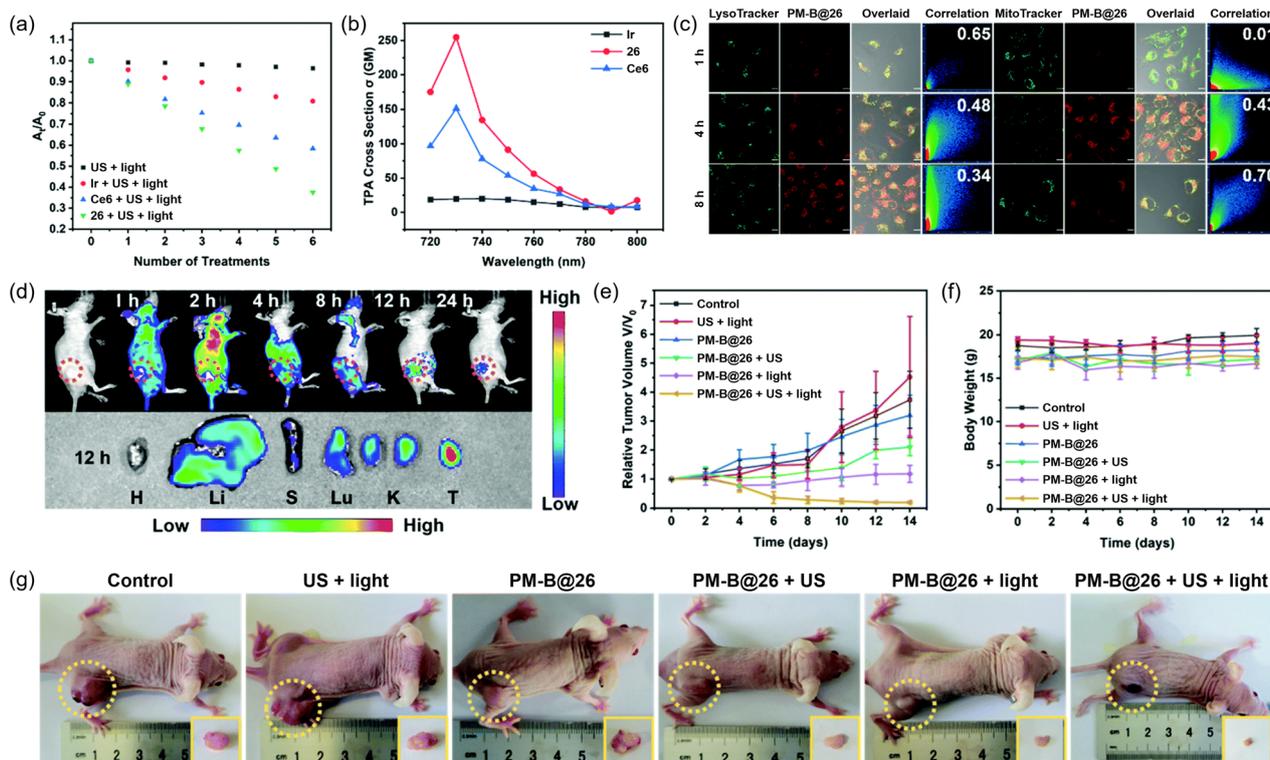
Fig. 7 (a) Changes in the absorption of 1,3-diphenylisobenzofuran (DPBF) (30 μM) at 416 nm in the presence of complex **26** (0.5 μM) or its individual components Ir and Ce6 (0.5 μM) upon exposure to US (1.0 MHz, 1.5 W cm^{-2}, 50% duty cycle, 2 min) and light irradiation (405 nm, 0.5 J cm^{-2}). (b) Two-photon absorption cross-section spectra of complex **26** (500 μM) or its individual components Ir and Ce6 (500 μM) in MeOH. (c) Time-dependent LSCM images of A375 cells incubated with **PM-B@26** ([Ir] = 1 μM) and co-stained with LysoTracker Green or MitoTracker Green. Scale bar = 10 μm. (d) Top: time-dependent *in vivo* luminescence images of an A375 tumour-bearing mouse after intravenous injection of **PM-B@26** (5 mg kg^{-1}). Bottom: *ex vivo* luminescence images of the major organs (H: heart, Li: liver, S: spleen, Lu: lungs, K: kidneys and T: tumour) dissected from the mouse 12 h post-intravenous injection of **PM-B@26**. (e and f) Changes in the (e) relative tumour volume and (f) body weights of A375 tumour-bearing mice after various treatments. (g) Representative photographs of A375 tumour-bearing mice after various treatments. US: 1.0 MHz, 1.5 W cm^{-2}, 50% duty cycle, 2 min; light: 730 nm, 35 mW, 5 min; **PM-B@26**: 5 mg kg^{-1}. Reproduced from ref. 88 with permission from the Royal Society of Chemistry, copyright 2022.

death through plasma membrane disruption and protein denaturation.[90] Notably, mild photothermal effects can enhance intratumoural blood flow and increase O$_2$ levels in tumour tissues, thereby sensitising tumours to SDT. Thus, the combination of SDT and PTT have considerable prospects for treating large solid tumours, particularly those with a hypoxic TME.

Black TiO$_2$ nanomaterials have attracted considerable attention as PTT agents due to their strong NIR absorption, high photothermal conversion efficiencies and excellent biocompatibility.[48] Chao and co-workers have modified black TiO$_2$ nanoparticles with an iridium(III) complex carrying a catechol unit (**28**) (Scheme 3) to afford a nanotherapeutic agent (**BTiO$_2$-28**) capable of producing ^{1}O$_2$ (Fig. 8a) and heat (Fig. 8b) upon exposure to US and NIR-II light, respectively, for combined SDT and PTT.[91] To impart tumour-targeting capabilities, **BTiO$_2$-28** is camouflaged with HeLa cell-derived membranes, yielding biomimetic nanoparticles (**BTiO$_2$-28@CM**) with homologous targeting and immune evasion properties for enhanced *in vivo* tumour accumulation. These nanoparticles exhibit preferential uptake by HeLa cells over other cancerous (A549, HepG2 and MCF-7) and non-cancerous (LO2 and murine macrophage RAW264.7) cell lines (Fig. 8c). After internalisation, they

primarily localise in the lysosomes and, upon lysosomal escape, gradually migrate to and accumulate in the mitochondria (Fig. 8d), driven by the cationic and lipophilic character of the iridium(III) complex. Upon dual US and NIR-II light irradiation, **BTiO$_2$-28@CM** induces significant mitochondrial dysfunction, leading to extensive cancer cell death. Additionally, **BTiO$_2$-28@CM** shows strong photoacoustic signals and photothermal effects upon NIR-II light exposure, allowing clear tumour visualisation in HeLa tumour-bearing mice *via* photoacoustic and photothermal imaging. Benefiting from cancer cell membrane camouflage, **BTiO$_2$-28@CM** displays prolonged blood circulation (Fig. 8e) and efficient tumour accumulation (Fig. 8f) post-intravenous injection. Importantly, the combined US and NIR-II light treatment achieves complete tumour eradication without causing systemic toxicity, resulting in 100% survival and no tumour recurrence over 60 days (group XI; Fig. 8g–i). This outcome surpasses those of SDT (group VIII) or PTT (group VII) alone with **BTiO$_2$-28@CM**, or combined SDT/PTT using non-targeted **BTiO$_2$** (group IX) or **BTiO$_2$-28** (group X), where incomplete tumour elimination leads to tumour relapse (Fig. 8g–i).

Gao and co-workers have designed a series of dinuclear ruthenium(II) complexes (**29**) (Scheme 3) as multimodal agents

Table 4 Summary of cytotoxic activity and applications of complexes **26–30** and their nanoformulations

Complex/nanoformulation	Cell line	$IC_{50,dark}$	$IC_{50,US+light}$	Irradiation conditions	Application	Ref.
PM-B@26	A375	>12 μM	0.40 μM	US: 1.0 MHz, 1.5 W cm^{-2}, 50% duty cycle, 2 min; light: 405 nm, 0.5 J cm^{-2}	SDT + PDT	88
	LO2	>12 μM	>12 μM			
27a	A549R	45.2 μM	2.65 μM 3.16 μM[a]	US: 1.0 MHz, 1.0 W cm^{-2}, 50% duty cycle; light: 808 nm, 100 mW cm^{-2}, 30.0 J cm^{-2}	SDT + PDT	89
27b		82.6 μM	4.36 μM 6.04 μM[a]			
27c		94.5 μM	4.57 μM 6.61 μM[a]			
27d		11.6 μM	0.249 μM 0.319 μM[a]			
27e		36.4 μM	0.624 μM 0.945 μM[a]			
27f		12.4 μM	0.118 μM 0.136 μM[a]			
BTiO$_2$-28@CM	HeLa	—	—	US: 1.0 MHz, 1.0 W cm^{-2}, 50% duty cycle, 1 min; light: 1064 nm, 1.0 W cm^{-2}, 5 min	SDT + PTT	91
29a	A549R	51.3 μM	1.10 μM 1.91 μM[b]	US: 1.0 MHz, 1.0 W cm^{-2}, 50% duty cycle; light: 808 nm, 100 mW cm^{-2}, 30.0 J cm^{-2}	SDT + PDT + PTT	92
29b		34.1 μM	0.745 μM 1.22 μM[b]			
29c		45.7 μM	0.510 μM 0.824 μM[b]			
29d		42.6 μM	0.487 μM 0.671 μM[b]			
29e		60.6 μM	0.846 μM 1.47 μM[b]			
29f		18.2 μM	0.184 μM 0.336 μM[b]			
29g		57.3 μM	0.121 μM 0.226 μM[b]			
29h		31.4 μM	0.247 μM 0.421 μM[b]			
30b	A549R	52.4 μM	0.322 μM 0.582 μM[b]	US: 1.0 MHz, 1.0 W cm^{-2}, 50% duty cycle, 5 min; light: 1064 nm, 200 mW cm^{-2}, 60.0 J cm^{-2}, 5 min	SDT + STT + PDT + PTT	93
30g		41.1 μM	0.0917 μM 0.142 μM[b]			
30i		34.6 μM	0.0285 μM 0.0513 μM[b]			

[a] The cells were cultured under hypoxia. [b] The cell culture plates were covered with a 1-mm thick layer of chicken breast on both the top and bottom to block light and US irradiation, respectively.

for treating cisplatin-resistant NSCLC *via* combined SDT, PDT and PTT.[92] The incorporation of a second metal centre enhances SOC and ISC, promoting triplet state formation for efficient ROS generation and photothermal conversion. These dinuclear complexes exhibit strong two-photon absorption (δ_{808nm} = 226–650 GM), allowing simultaneous two-photon-induced PDT and PTT using an 808-nm laser. Unlike traditional PTT agents that rely on significant temperature increase, these complexes show modest photothermal conversion efficiencies (η_{808nm} = 3.0–3.9%) and induce only mild temperature increases (3–6 °C) upon irradiation at 808 nm. This mild photothermal effect is beneficial for enhancing SDT and PDT while reducing the risks of causing thermal damage to surrounding normal tissues. The complexes are taken up by A549R cells *via* macropinocytosis and predominantly enriched in the mitochondria with partial nuclear localisation, which enables DNA interaction and thereby results in moderate dark cytotoxicity ($IC_{50,dark}$ = 18.2–60.6 μM; Table 4). Upon US (1.0 MHz, 1.0 W cm^{-2}, 50% duty

cycle) and NIR-I light (808 nm, 100 mW cm^{-2}, 30.0 J cm^{-2}) exposure, their cytotoxic activity is dramatically increased ($IC_{50,US+light}$ = 0.121–1.10 μM), which remains effective ($IC_{50,US+light}$ = 0.226–1.91 μM) even with a 1-mm chicken breast covering both sides of the culture plate, demonstrating the deep tissue penetration capabilities of US and NIR light. Remarkably, this combined treatment induces significant tumour regression in A549R tumour-bearing mice with minimal hepatic or renal toxicity due to efficient clearance of the complexes post-treatment, achieving a 100% survival rate at the end of the experiment.

Chen, Ren, Cheng, Gao and co-workers have developed a series of non-emissive ruthenium(ii) complexes (**30**) (Scheme 3) as single-molecule multimodal agents for US- and NIR-II light-mediated therapies.[93] These complexes feature distinct structural modifications, including the incorporation of: (1) heavy atoms such as bromine to enhance ISC, (2) electron-donating groups such as methoxy groups to improve ROS
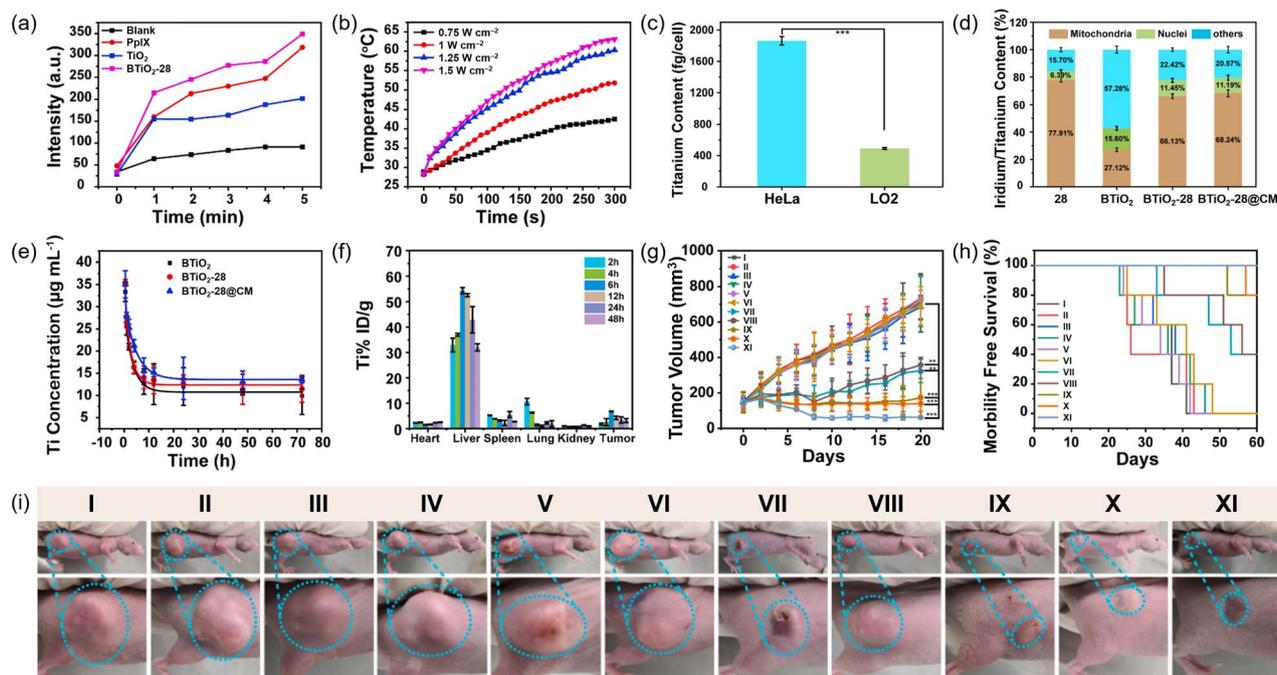
Fig. 8 (a) Time-dependent changes in the fluorescence intensity of DCF (0.4 μM) at 523 nm in the presence of PpIX (100 ppm), TiO$_2$ ([Ti] = 100 ppm) or BTiO$_2$-28 ([Ti] = 100 ppm) upon US irradiation (1.0 MHz, 1.0 W cm^{-2}, 50% duty cycle) for 0, 1, 2, 3, 4 and 5 min. (b) Changes in temperature of an aqueous solution of BTiO$_2$-28 ([Ti] = 100 ppm) upon irradiation at 1064 nm at various power densities (0.75, 1, 1.25 and 1.5 W cm^{-2}) for 5 min. (c) Intracellular titanium content in HeLa and LO2 cells after incubation with BTiO$_2$-28@CM ([Ti] = 100 ppm, 8 h), as determined by inductively coupled plasma-mass spectrometry (ICP-MS) measurements. (d) Subcellular distribution of complex 28, BTiO$_2$, BTiO$_2$-28 and BTiO$_2$-28@CM ([Ti] = 100 ppm) in HeLa cells after incubation for 8 h, as determined by ICP-MS measurements. (e) Blood circulation time of BTiO$_2$, BTiO$_2$-28 and BTiO$_2$-28@CM (10 mg kg^{-1}) in HeLa tumour-bearing mice after intravenous injection. (f) Biodistribution of BTiO$_2$-28@CM (10 mg kg^{-1}) in HeLa tumour-bearing mice at various time points (2, 4, 6, 12, 24 and 48 h) after intravenous injection, as determined by ICP-MS measurements. (g) Tumour growth curves and (h) survival rates of HeLa tumour-bearing mice after various treatments. (i) Representative photographs of the tumour region in HeLa tumour-bearing mice after various treatments. Group I: saline; II: light; III: US; IV: BTiO$_2$; V: BTiO$_2$-28; VI: BTiO$_2$-28@CM; VII: BTiO$_2$-28@CM + light; VIII: BTiO$_2$-28@CM + US; IX: BTiO$_2$ + light + US; X: BTiO$_2$-28 + light + US; XI: BTiO$_2$-28@CM + light + US. Light: 1064 nm, 1.0 W cm^{-2}, 10 min; US: 1.0 MHz, 1.0 W cm^{-2}, 50% duty cycle, 5 min; BTiO$_2$, BTiO$_2$-28 or BTiO$_2$-28@CM: 10 mg kg^{-1}. Reproduced from ref. 91 with permission from Elsevier, copyright 2021.

sensitisation and (3) hydrophobic ligands such as di-*tert*-butyl- or diphenyl-substituted acetylacetonate to promote cellular uptake. Computational studies suggest that these complexes possess a low-lying triplet excited state (1.02–1.15 eV), favouring non-radiative relaxation. Notably, the bromo-substituted complexes 30b, 30g and 30i display the largest two-photon absorption cross-sections (δ_{1064nm} = 672, 9.22 $\times$ 10^3 and 1.05 $\times$ 10^4 GM, respectively), enabling simultaneous PDT and PTT with NIR-II light that offers deeper tissue penetration. Upon irradiation with a 1064-nm laser, these complexes efficiently generate ROS and heat (η_{1064nm} = 18–22%). Remarkably, they also induce temperature increases upon sonoexcitation, supporting sonothermal therapy (STT) alongside SDT, PDT and PTT. Thus, complexes 30b, 30g and 30i exhibit potent cytotoxicity towards A549R cells (IC$_{50,US+light}$ = 0.0285–0.322 μM; Table 4) upon simultaneous US (1.0 MHz, 1.0 W cm^{-2}, 50% duty cycle, 5 min) and NIR-II light (1064 nm, 200 mW cm^{-2}, 60.0 J cm^{-2}, 5 min) exposure. Mechanistic investigations show that complex 30i is primarily internalised into the cells *via* a macropinocytic pathway and enriched in the mitochondria after cellular uptake. Upon dual US and NIR-II light irradiation, it induces both apoptosis and ferroptosis *via* ROS and heat production. *In vivo*

studies reveal that the sono- and photothermal conversion effects of complex 30i can soften and swell the tumour tissues, increasing vascular permeability and intratumoural O$_2$ availability, thereby enhancing SDT and PDT efficacy. The combined SDT, STT, PDT and PTT lead to complete tumour ablation and 100% survival in A549R tumour-bearing mice with no observable side effects.

3. Transition metal complexes in sonodynamic therapy for microbial infections

Microbial infections pose a serious threat to global human health due to the emergence of antimicrobial resistance.[94] A key contributor to this resistance is the formation of biofilms, which are structured microbial communities that adhere to surfaces and are encased in a self-produced matrix of extracellular polymeric substances.[95] This biofilm microenvironment (BME) not only protects microbes from host immune defences but also hinders the penetration and efficacy of antimicrobial agents. As a result, microbes within biofilms display enhanced

tolerance to conventional treatments, allowing them to survive under hostile conditions, persist within the host and disperse to colonise new sites. Thus, there is an urgent need for innovative and effective therapeutic strategies that can target and eliminate microbial biofilms without promoting further antimicrobial resistance.

Zhang and co-workers have designed a TPE-appended rhenium(I) tricarbonyl complex (**31**) (Scheme 4) that acts as both a $^1O_2$ sonosensitiser and a sonoCORM for treating mycobacterium biofilm-associated infections *via* combined SDT and CO gas therapy.[96] Owing to the AIE-active TPE moiety, the complex exhibits enhanced emission and $^1O_2$ sonosensitisation upon aggregation in aqueous media. Similar to other rhenium(I)-based sonoCORMs, the axial CO ligand is released from the complex upon US exposure. Thus, the complex shows potent antibacterial activity against Gram-negative *Escherichia coli* (*E.*

coli) and *Mycobacterium smegmatis* (*M. smegmatis*) (MIC$_{US}$ = 6.25 and 12.5 μM, respectively; Table 5) upon irradiation with US (1.0 MHz, 1.0 W cm^{-2}, 50% duty cycle, 10 min), as the simultaneous generation of $^1O_2$ and CO severely damages the bacterial membranes, leading to extensive bacterial cell death. Metabolomic analysis reveals that the treatment also disturbs purine metabolism of the bacteria, impairing DNA synthesis and energy metabolism. Importantly, the complex effectively eradicates *E. coli* and *M. smegmatis* biofilms upon US stimulation, reducing their viability to 39.5 and 37.2%, respectively. Notably, the complex displays negligible antibacterial activity against Gram-positive bacteria (MIC$_{US}$ > 25 μM for *Staphylococcus aureus* (*S. aureus*)) and low cytotoxicity towards mammalian cells (IC$_{50,US}$ > 50 μM for murine fibroblast NIH/3T3 and L929 cells) upon US triggering, indicative of its high selectivity for Gram-negative bacteria and biofilms.

Sun and co-workers have developed a ruthenium(II)-based metallacycle (**32**) (Scheme 4) that functions as a BME-adaptive ROS sonosensitiser and sonocatalyst to combat multidrug-resistant bacterial biofilms.[97] This [2 + 2] metallacycle is constructed *via* the coordination-driven self-assembly between a 4,6-di(2-thienyl)thieno[3,4-*c*][1,2,5]thiadiazole (TTD) derivative that serves as a ditopic donor and a dinuclear *p*-cymene ruthenium(II) 5,8-dioxido-1,4-naphtoquinonato complex that acts as an acceptor. The TTD ligand endows the metallacycle with strong NIR luminescence at 880 nm (Fig. 9a), facilitating *in vivo* imaging and image-guided SDT. Additionally, the ruthenium(II) acceptor efficiently produces $^1O_2$ upon US exposure. Thus, the metallacycle exhibits superior ROS generation efficiency compared to commercial sonosensitisers such as PpIX, indocyanine green (ICG), 5-ALA, Ce6, methylene blue (MB) and [Ru(bpy)$_3$]$^{2+}$ (Fig. 9b). Notably, the metallacycle possesses both catalase- and peroxidase-like activity, catalysing the decomposition of endogenous H_2O_2 into O_2 and HO$^•$ (Fig. 9c and d), respectively. This helps modulate the hypoxic BME and sustains ROS production. Furthermore, the metallacycle triggers the oxidation of GSH to glutathione disulfide and, upon US stimulation, promotes the oxidation of NADPH to NADP$^+$, thereby disrupting intracellular redox balance and weakening bacterial antioxidant defence. As a result, the metallacycle shows potent
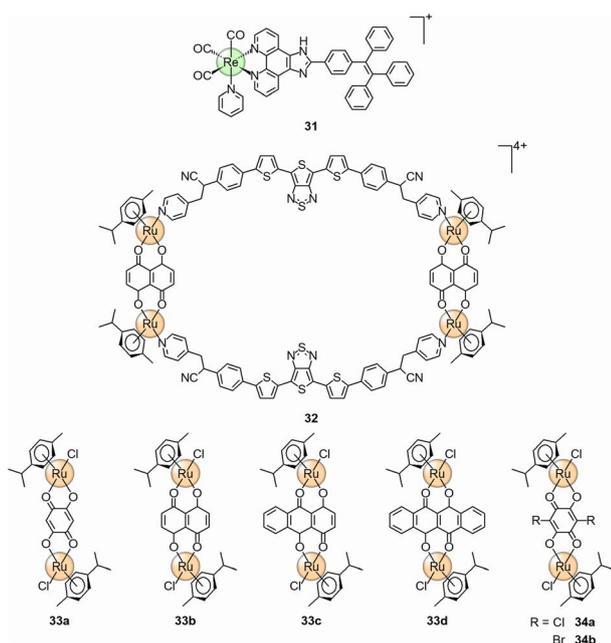
Scheme 4 Structures of complexes **31–34**.

Table 5 Summary of antimicrobial activity and applications of complexes **31–34**

Complex	Microbial strain	MIC$_{dark}$	MIC$_{US}$	Irradiation conditions	Application	Ref.
31	*E. coli*	>25 μM^a	6.25 μM^a	1.0 MHz, 1.0 W cm^{-2}, 50% duty cycle, 10 min	SDT + CO gas therapy	96
	M. smegmatis	>25 μM^a	12.5 μM^a			
	S. aureus	>25 μM^a	>25 μM^a			
32	MRSA	5 μM	0.63 μM	1.0 MHz, 1.0 W cm^{-2}, 50% duty cycle, 5 min	SDT	97
	Multidrug-resistant *E. coli*	7.5 μM	2.5 μM			
33d	*E. coli*	>20 μM^b	>20 μM^b	1.0 MHz, 1.0 W cm^{-2}, 50% duty cycle, 5 min	SDT	98
	MRSA	>10 μM^b	<2.5 μM^b			
34a	*C. albicans*	>40 μM^c	10 μM^c	1.0 MHz, 1.0 W cm^{-2}, 50% duty cycle, 5 min	SDT	99
	C. glabrata	>40 μM^c	20 μM^c			
34b	*C. albicans*	>40 μM^c	5 μM^c			
	C. glabrata	>40 μM^c	5 μM^c			

^{a} Concentration of the complex that inhibits >90% of microbial growth. ^{b} Concentration of the complex that inhibits 50% of microbial growth. ^{c} Concentration of the complex that completely inhibits microbial growth.
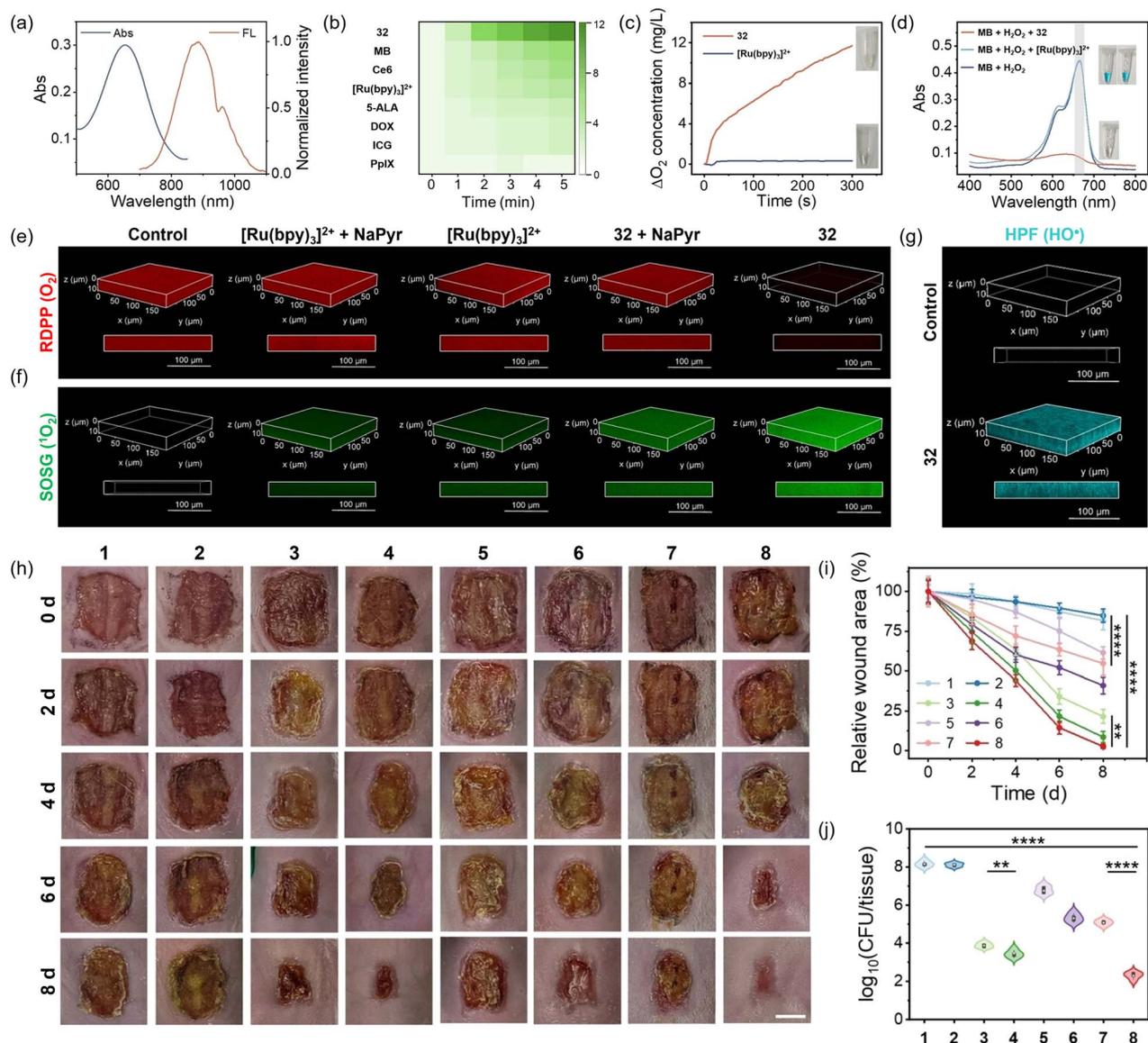
Fig. 9 (a) Absorption and normalised emission spectra of complex **32** in DMSO. (b) Heat map of relative fluorescence intensity changes of DCFH (20 μM) at 525 nm in the presence of complex **32** (20 μM) or other commercial sonosensitisers (20 μM) in DMF upon US irradiation (1.0 MHz, 1.0 W cm^{-2}, 50% duty cycle) for 0, 1, 2, 3, 4 and 5 min. (c) Changes in O$_2$ concentration after incubation of H$_2$O$_2$ (1 mM) with complex **32** or [Ru(bpy)$_3$]$^{2+}$ (10 μM) in NaAc–HAc buffer (pH = 6.5). Insets: photos of relevant tubes after various treatments. (d) UV-vis absorption spectra and photos of relevant tubes (inset) of MB (80 μM) in the presence of H$_2$O$_2$ (10 mM) upon incubation with complex **32** or [Ru(bpy)$_3$]$^{2+}$ (20 μM) in NaAc–HAc buffer (pH = 6.5) for 2 h. (e–g) 3D LSCM images of multidrug-resistant *E. coli* biofilms incubated with complex **32** or [Ru(bpy)$_3$]$^{2+}$ (10 μM, 9 h) with or without pretreatment of the H$_2$O$_2$ scavenger sodium pyruvate (NaPyr) (10 mM, 1 h), and then stained with (e) the O$_2$-sensitive probe [Ru(dpp)$_3$]$^{2+}$ (RDPP) (dpp = 4,7-diphenyl-1,10-phenanthroline) (10 μg mL^{-1}, 30 min), (f) the ^{1}O$_2$-sensitive probe SOSG (20 μM, 30 min), or (g) the HO$^{\bullet}$-sensitive probe hydroxyphenyl fluorescein (HPF) (10 μM, 30 min). (h) Photographs of the wound area in mice with multidrug-resistant *E. coli* biofilm-infected wounds after various treatments. Scale bar = 0.5 cm. (i) Relative wound area in the mice after various treatments. (j) Violin plots show the bacterial count in the wounds at day 8 post-treatment. Group 1: PBS; 2: PBS + US; 3: Van; 4: TIG; 5: [Ru(bpy)$_3$]$^{2+}$; 6: [Ru(bpy)$_3$]$^{2+}$ + US; 7: complex **32**; 8: complex **32** + US. US: 1.0 MHz, 1.0 W cm^{-2}, 50% duty cycle, 5 min; Van, TIG, [Ru(bpy)$_3$]$^{2+}$ or complex **32**: 300 μM. **p < 0.01 and ****p < 0.0001. Reproduced from ref. 97 with permission from Wiley-VCH, copyright 2024.

sonoinduced antibacterial activity against methicillin-resistant *S. aureus* (MRSA) and multidrug-resistant *E. coli* (MIC$_{US}$ = 0.63 and 2.5 μM, respectively; Table 5) by compromising bacterial membrane integrity, while displaying negligible cyto-toxicity towards mammalian cells (IC$_{50,US}$ > 80 μM for human normal bronchial epithelial BEAS-2B cells). The metallacycle also effectively penetrates and accumulates in multidrug-

resistant *E. coli* biofilms, alleviates hypoxia and impairs anti-oxidant defence in the BME, facilitating ROS-mediated biofilm eradication (Fig. 9e–g). *In vivo* studies demonstrate that treatment of biofilm-infected wounds in mice with the metallacycle and US irradiation results in complete wound healing with negligible inflammation (Fig. 9h–j), outperforming clinical antibiotics such as vancomycin (Van) and tigecycline (TIG) as

well as conventional sonosensitisers such as $[Ru(bpy)_3]^{2+}$ with a wound healing rate of *ca.* 78, 91 and 59%, respectively.

Li, Sun, Li and co-workers have investigated dinuclear *p*-cymene ruthenium(II) complexes (33) (Scheme 4) as sonosensitisers for SDT.[98] Among them, complex **33d** exhibits the highest $^1O_2$ generation efficiency upon US triggering, attributed to its largest π-conjugation plane that significantly reduces the HOMO–LUMO gap (0.77 eV) for sonoactivation and ROS sensitisation. It also efficiently catalyses the decomposition of H_2O_2 into O_2 and $HO^{\bullet}$ as well as the oxidation of GSH and NADPH, further amplifying the oxidative stress. Its multiple modes of action lead to potent antibacterial activity against MRSA and its biofilms, enabling complete recovery in mice with MRSA biofilm-infected wounds.

Based on these dinuclear *p*-cymene ruthenium(II) scaffolds, Qiu, Chen, Xing, Sun and co-workers have developed two new ruthenium(II) complexes (34) (Scheme 4) using a heavy atom engineering approach for treating fungal infections.[99] Compared to the parent complex **33a**, the incorporation of two chlorine or bromine atoms into the 2,5-dioxido-1,4-benzoquinonato ligand substantially lowers the S_1–T_1 energy gap of complexes **34a** and **34b** from 0.365 eV to 0.251 and 0.202 eV, respectively, enhancing ISC and thereby improving $^1O_2$ sonosensitisation. Notably, complex **34b** is inactive in the dark ($MIC_{dark} > 40$ μM) but shows potent antifungal activity against *Candida albicans* (*C. albicans*) and *Candida glabrata* (*C. glabrata*) ($MIC_{US} = 5$ μM) upon exposure to US (1.0 MHz, 1.0 W cm^{-2}, 50% duty cycle, 5 min) (Table 5), comparable to the first-line clinical antifungal drug amphotericin B ($MIC_{dark} = 5$ μM), while maintaining low (sono)cytotoxicity towards mammalian cells ($IC_{50} > 80$ μM for L929 cells). Mechanistic studies show that the accumulation of the complex on fungal cell membrane triggers membrane rupture, while its US-mediated ROS production inside the cells disrupts MMP and depletes ATP, resulting in fungal cell death. Importantly, treatment of *C. albicans*-infected mice with complex **34b** and US irradiation significantly reduces fungal burden at the wound site and restores subcutaneous tissue function without causing adverse effects on the liver or kidney, surpassing amphotericin B that is known for its nephrotoxicity.

4. Transition metal complexes in sonodynamic therapy for cardiovascular diseases

Cardiovascular diseases are a leading cause of death and disability worldwide.[100] Common manifestations include myocardial infarction and ischemic stroke, both resulting from thrombosis that obstructs blood flow to the heart or brain, depriving tissues of O_2 and nutrients and causing irreversible damage. Standard treatments involve the use of antithrombotic agents such as anticoagulants and antiplatelet drugs to restore blood circulation, or surgical interventions like angioplasty or bypass surgery in severe cases. However, antithrombotic agents often face high risks of bleeding complications.[101] Additionally, thrombus dissolution can trigger inflammation, further

promoting platelet aggregation and thrombus growth.[102] These challenges underscore the urgent need for safer and more effective therapeutic alternatives.

Zhang, Zhu, Bryce, Ren, Tang and co-workers have designed a US-activatable nanoplatform (**PM-R@35/N₃-BTC**) for thrombolytic therapy.[103] This nanoplatform comprises: (1) a mononuclear (**35a**) or tetranuclear iridium(III) porphyrin complex (**35b**) (Scheme 5) that acts as both an ROS sonosensitiser and a bioorthogonal sonocatalyst, and (2) an azide-functionalised benzylthiocarbamate (**N₃-BTC**) that serves as a hydrogen sulfide (H₂S) donor. These components are encapsulated into micelles modified with cyclic RGD peptides, which target integrin $\alpha_{IIb}\beta_3$ overexpressed on platelets for thrombus-specific delivery. Compared to the AIE-inactive mononuclear complex **35a**, the tetranuclear complex **35b** displays enhanced NIR emission as well as $^1O_2$ and $HO^{\bullet}$ generation in aqueous media (Fig. 10a). It also exhibits superior catalytic activity in reducing the azide moiety of **N₃-BTC** upon US exposure, triggering the release of H₂S from the nanoplatform (Fig. 10b). The released H₂S mitigates inflammation by inhibiting pro-inflammatory cytokines such as tumour necrosis factor-α and interleukin-6, as well as transcription factors such as nuclear factor-κB, thereby preventing thrombus reformation after SDT. Additionally, the multimetallic structure of complex **35b** enhances its reactivity towards peroxynitrite ($ONOO^-$), giving rise to intense and long-lasting (>10 min) NIR chemiluminescence (Fig. 10c and d) detectable at a tissue depth of 12 mm with a high signal-to-background ratio (12.15). This enables high-contrast thrombus imaging *in vivo*, revealing that **PM-R@35b/N₃-BTC**
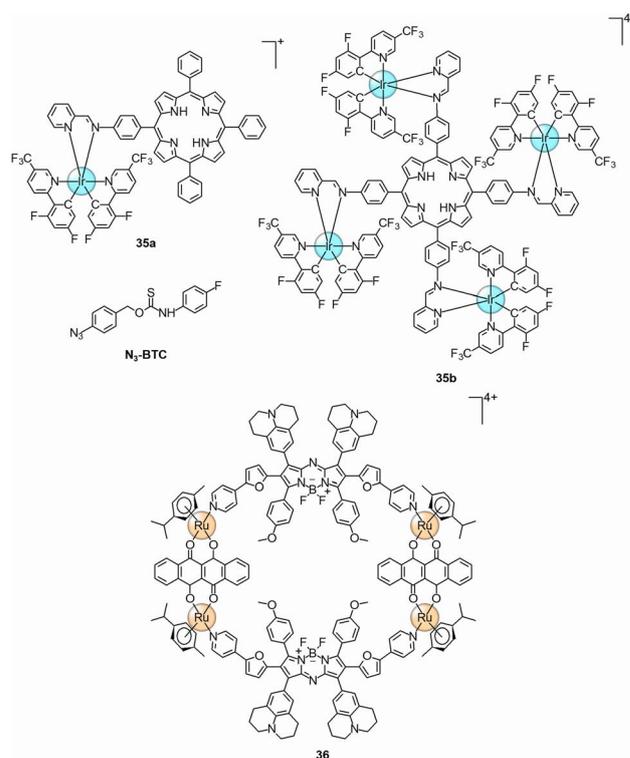
Scheme 5 Structures of complexes 35 and 36.

accumulates at the thrombus site within 1 h post-injection in mice with carotid artery thrombus (Fig. 10e). Importantly, US irradiation at the thrombus site achieves a thrombolysis rate of 91%, restoring ca. 77% blood flow with minimal haemorrhagic risk (Fig. 10f–i). This performance surpasses that of the clinical thrombolytic drug urokinase (uPA), which suffers from rapid clearance and a high risk of bleeding, leading to thrombus reformation within 30 min (Fig. 10h). Similar therapeutic outcomes are observed in a rat model of femoral vein thrombosis (Fig. 10j), highlighting the synergistic benefits of SDT and H_2S release in achieving thrombus ablation and vascular recanalisation.

Sun and co-workers have developed an NIR-emissive ruthenium(II)-based metallacycle (**36**) (Scheme 5) for modulating myocardial infarction-induced ventricular arrhythmias via SDT.[104] This metallacycle efficiently produces various types of ROS including $^1O_2$, $O_2^{\bullet-}$ and $HO^{\bullet}$ upon US stimulation. As shown by LSCM, the metallacycle is efficiently taken up by murine microglial BV2 cells and enriched in the mitochondria. Notably, the metallacycle enhances cell survival at a low concentration (5 μM) and US power (0.5 W cm^{-2}) by triggering mitochondrial autophagy, while inducing cell apoptosis at higher doses (>5 μM) and elevated US power (>0.5 W cm^{-2}) (Table 6). To increase its biocompatibility for in vivo applications, the metallacycle has been encapsulated into liposomes. In vivo luminescence imaging reveals that the resultant nanoparticles (**LP@36**) show prolonged retention (>12 h) in the paraventricular nucleus of a rat model of myocardial infarction
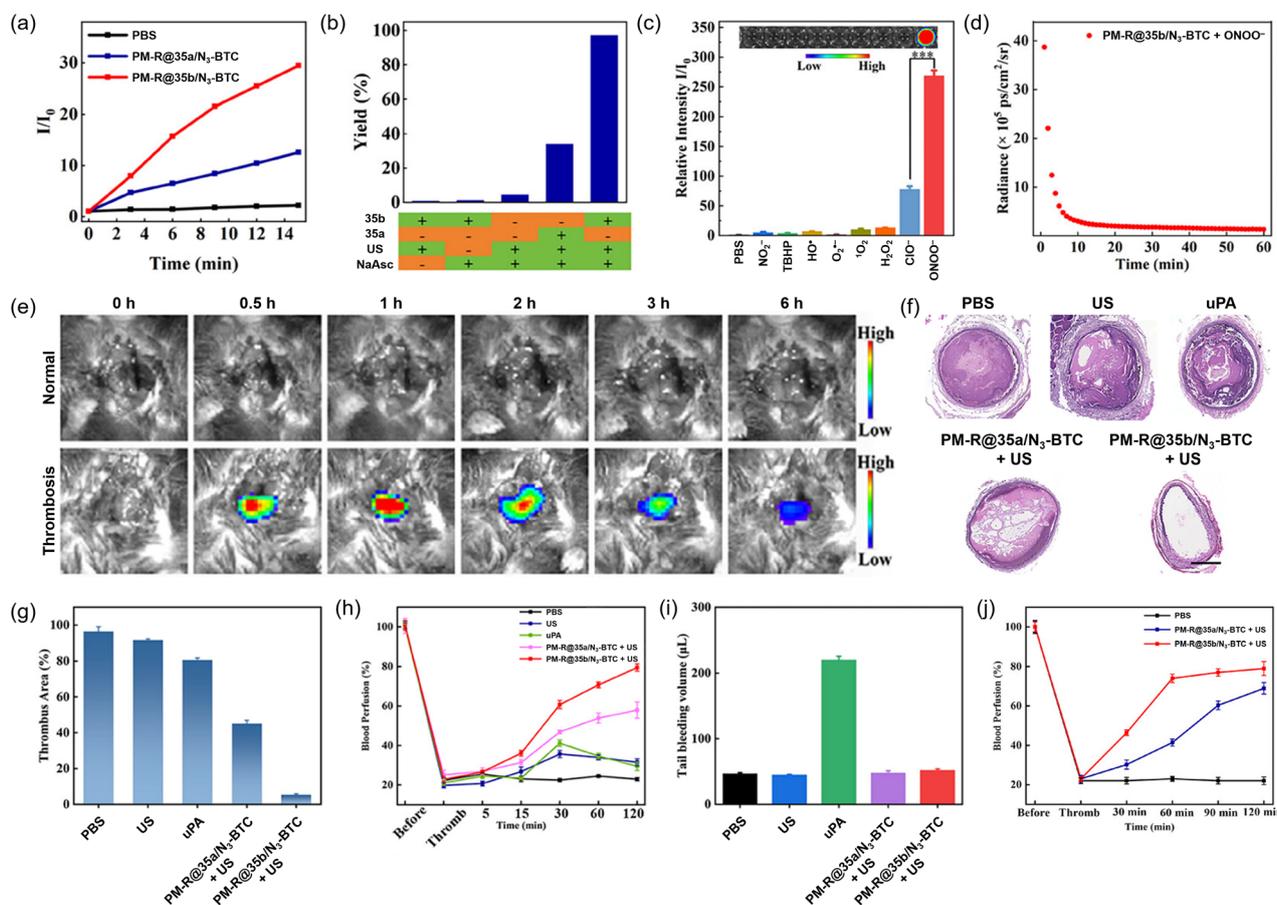

Fig. 10 (a) Time-dependent changes in the fluorescence intensity of DCFH at 525 nm in the presence of **PM-R@35a/N₃-BTC** or **PM-R@35b/N₃-BTC** upon US irradiation (1.0 MHz, 1.0 W cm^{-2}, 50% duty cycle) for 0, 3, 6, 9, 12 and 15 min. (b) Yields of reduction of rhodamine bisazide 1 (40 μM) in the presence of sodium ascorbate (NaAsc) (2 mM) catalysed by complex **35a** or **35b** (5 μM) under US irradiation (1.0 MHz, 1.0 W cm^{-2}, 50% duty cycle). (c) Chemiluminescence intensity of **PM-R@35b/N₃-BTC** (100 μg mL^{-1}) in PBS in the absence and presence of different reactive oxygen and nitrogen species (200 μM), including nitrite (NO_2^-), tert-butyl hydroperoxide (TBHP), $HO^{\bullet}$, $O_2^{\bullet-}$, $^1O_2$, H_2O_2, hypochlorite (ClO^-) and $ONOO^-$. Inset shows the corresponding chemiluminescence images acquired by an in vivo imaging system (IVIS) under bioluminescence mode with an open filter. ***p < 0.001. (d) Decay of chemiluminescence signal of **PM-R@35b/N₃-BTC** over time at room temperature after addition of $ONOO^-$. (e) IVIS images of the carotid artery site in a normal mouse (top) and a mouse with carotid thrombosis (bottom) at different time intervals post-injection of **PM-R@35b/N₃-BTC** (5 mg kg^{-1}). (f) Hematoxylin−eosin staining images of the carotid arteries excised from mice with carotid thrombosis after various treatments. Scale bar = 300 μm. (g) Quantification of the thrombus area in the mouse carotid artery after various treatments. (h) Relative blood perfusion of the mouse carotid artery after FeCl₃ induction and various treatments. (i) The mouse tail bleeding volume after various treatments. (j) Relative blood perfusion of the rat femoral vein after FeCl₃ induction and various treatments. US: 1.0 MHz, 1.0 W cm^{-2}, 50% duty cycle, 2 h; uPA: 0.04 mg kg^{-1}; **PM-R@35a/N₃-BTC** and **PM-R@35b/N₃-BTC**: 5 mg kg^{-1}. Reproduced from ref. 103 with permission from Wiley-VCH, copyright 2025.

Table 6 Summary of cytotoxic activity and applications of nanoformulations of complexes 35 and 36

Nanoformulation	Cell line	$IC_{50,dark}$	$IC_{50,US}$	Irradiation conditions	Application	Ref.
PM-R@35a/N$_3$-BTC	HUVEC	200 µg mL^{-1}	—	—	SDT + H$_2$S gas therapy	103
PM-R@35b/N$_3$-BTC	HUVEC	200 µg mL^{-1}	—			
LP@36	BV2	>7.5 µM	>15 µM	1.0 MHz, 0.5 W cm^{-2}, 50% duty cycle, 5 min	SDT	104
		>7.5 µM	<7.5 µM	1.0 MHz, 1.0 W cm^{-2}, 50% duty cycle, 5 min		

after microinjection. Importantly, when US is applied to the skull surface 12 h post-injection, ROS are generated in the paraventricular nucleus, suppressing the activation of central microglia during neuroinflammation. This reduces sympathetic activity in both the central nervous system and left stellate ganglion, significantly lowering the incidence of ventricular arrhythmias. Furthermore, no tissue damage is observed in the brain or other major organs after the treatment, supporting SDT as a promising strategy for mitigating ventricular arrhythmias.

5. Conclusions

In this review, we summarise the recent development of US-activatable transition metal complexes for SDT. These complexes possess attractive properties as SDT agents, including high ROS generation efficiencies, strong catalytic activity and excellent stability under US exposure. Coupled with the deep tissue penetration of US, these complexes have shown significant potential in treating various conditions, including cancer, microbial infections and cardiovascular diseases, particularly in areas inaccessible to light. Despite these exciting developments, several challenges remain that must be addressed to facilitate their clinical translation, especially given the pivotal role of ROS sonosensitisers in SDT.

A major limitation for current transition metal-based ROS sonosensitisers is their strong reliance on O$_2$ to produce ROS, particularly ^{1}O$_2$, resulting in diminished therapeutic efficacy under hypoxia, a common feature of many pathological environments such as solid tumours, microbial biofilms and thrombi. One effective way to overcome this limitation is by developing sonosensitisers that generate ROS such as O$_2^{\cdot-}$, which can initiate cascade biochemical reactions (e.g., superoxide dismutase-mediated disproportionation reaction as well as Fenton and Haber–Weiss reaction), regenerating O$_2$ for sustained ROS production even in O$_2$-depleted environments. This can be achieved by introducing electron donor and acceptor moieties into the complexes to modulate their triplet state energy levels, thereby suppressing ^{1}O$_2$ generation via the type II pathway while favouring the production of other ROS via the type I pathway. Also, the development of novel transition metal complexes as efficient sonocatalysts for redox reactions, such as NADH oxidation, offers an additional route to counteract hypoxia-induced therapeutic resistance by disrupting intracellular redox homeostasis. An alternative approach is to remodel the hypoxic microenvironments by using nanocarriers (e.g.,

perfluorocarbons and micro/nanobubbles) to deliver exogenous O$_2$ to the target tissues, or by employing O$_2$-evolving nanomaterials to convert endogenous H$_2$O$_2$ (e.g., MnO$_2$ nanoparticles and catalase-mimicking nanozymes) or water (e.g., TiO$_2$ nanoparticles and C$_3$N$_4$ nanocomposites) into O$_2$ in situ. Furthermore, integrating SDT with O$_2$-independent therapies such as immunotherapy, chemotherapy, gas therapy, SACT and PTT is expected to further enhance therapeutic outcomes.

Another major challenge is the low selectivity of ROS sonosensitisers for diseased tissues, which often leads to non-specific accumulation in healthy tissues, increasing the risk of collateral damage and acute toxicity. To address this issue, ROS sonosensitisers can be functionalised with targeting units such as peptides, antibodies or aptamers, or encapsulated into nanocarriers with targeting capabilities to improve their localisation at disease sites and minimise off-target effects, thereby enhancing the therapeutic efficacy. Additionally, the development of activatable ROS sonosensitisers and sonocatalysts responsive to disease-specific biomarkers offers an exciting strategy for enhancing treatment precision through targeted activation.

Beyond their therapeutic role, transition metal-based ^{1}O$_2$ sonosensitisers also possess great potential for diagnostic applications. For example, they can be utilised in the design of sonoafterglow probes, serving as an initiator to convert organic afterglow substrates such as adamantylidenes into unstable dioxetane derivatives that emit light upon decomposition.[105] This light can be transferred back to the sonosensitiser and trigger a self-sustained luminescence process, resulting in long-lasting afterglow luminescence that facilitates high-contrast, background-free imaging. Their dual functional roles pave the way for the development of theranostic platforms that combine disease diagnosis and treatment and provide real-time feedback for treatment response, offering an attractive avenue towards precision medicine.

In conclusion, it is important to note that the exact mechanisms underlying SDT remain elusive, posing significant challenges to establishing clear guidelines for the rational design of next-generation sonosensitisers. Further mechanistic understanding is essential to advance their development. Nevertheless, systematic studies on structure–activity relationships will play an important role in guiding the design of more effective agents with greater clinical potential. Additionally, the optimisation and standardisation of key US parameters, including frequency, intensity, duty cycle and treatment duration, are

critical for improving the reproducibility and clinical translatability of SDT. These efforts will enhance the evaluation of sonosensitiser performance and accelerate the identification of potential clinical candidates. Nevertheless, US-activatable transition metal complexes represent a promising yet still emerging class of SDT agents. Continued research and innovation in their molecular designs are crucial for overcoming current challenges, enhancing therapeutic performance and promoting clinical translation. These advancements are expected to broaden their biomedical applications and facilitate the clinical adoption of SDT for improving patient outcomes.

Author contributions

L. C.-C. L. performed literature search and wrote the original draft of the manuscript. L. C.-C. L. and K. K.-W. L. revised and finalised the manuscript.

Conflicts of interest

There are no conflicts to declare.

Data availability

No primary research results, software or code have been included and no new data were generated or analysed as part of this review.

Acknowledgements

References

1 D. E. J. G. J. Dolmans, D. Fukumura and R. K. Jain, *Nat. Rev. Cancer*, 2003, **3**, 380–387.

2 T. C. Pham, V.-N. Nguyen, Y. Choi, S. Lee and J. Yoon, *Chem. Rev.*, 2021, **121**, 13454–13619.

3 V.-N. Nguyen, Z. Zhao, B. Z. Tang and J. Yoon, *Chem. Soc. Rev.*, 2022, **51**, 3324–3340.

4 Y. Xu, H. Xiong, B. Zhang, I. Lee, J. Xie, M. Li, H. Zhang and J. S. Kim, *Coord. Chem. Rev.*, 2022, **470**, 214726.

5 W. Fan, P. Huang and X. Chen, *Chem. Soc. Rev.*, 2016, **45**, 6488–6519.

6 J. R. Lindner, *Nat. Rev. Drug Discovery*, 2004, **3**, 527–533.

7 S. Mitragotri, *Nat. Rev. Drug Discovery*, 2005, **4**, 255–260.

8 X. Lin, J. Song, X. Chen and H. Yang, *Angew. Chem., Int. Ed.*, 2020, **59**, 14212–14233.

9 N. Yumita, R. Nishigaki, K. Umemura and S.-i. Umemura, *Jpn. J. Cancer Res.*, 1989, **80**, 219–222.

10 X. Xing, S. Zhao, T. Xu, L. Huang, Y. Zhang, M. Lan, C. Lin, X. Zheng and P. Wang, *Coord. Chem. Rev.*, 2021, **445**, 214087.

11 Y. Ding, Y. Yang, O. Aras, F. An, M. Zhou and Y. Chai, *Aggregate*, 2025, **6**, e70032.

12 D. Li, Y. Zhu, W. Yin, X. Lin, G. Kim, Z. Liu, S. Jung, J. Seo, S. Kim, J. S. Kim, H. Huang and P. Zhang, *Chem. Soc. Rev.*, 2025, **54**, 7610–7653.

13 Z. He, J. Du, Y. Miao and Y. Li, *Adv. Healthcare Mater.*, 2023, **12**, 2300234.

14 X. Cao, M. Li, Q. Liu, J. Zhao, X. Lu and J. Wang, *Small*, 2023, **19**, 2303195.

15 W. Qin, Q. Yang, C. Zhu, R. Jiao, X. Lin, C. Fang, J. Guo and K. Zhang, *Small*, 2024, **20**, 2311228.

16 J. Chen, Q. Zhou and W. Cao, *Adv. Funct. Mater.*, 2024, **34**, 2405844.

17 F. Yang, J. Dong, Z. Li and Z. Wang, *ACS Nano*, 2023, **17**, 4102–4133.

18 Z. Chen, X. Wu, J. Liang and H. Chao, *Coord. Chem. Rev.*, 2024, **521**, 216169.

19 Z. Liu, X. Lin, H. Wang and P. Zhang, *Coord. Chem. Rev.*, 2025, **544**, 216969.

20 L. K. McKenzie, H. E. Bryant and J. A. Weinstein, *Coord. Chem. Rev.*, 2019, **379**, 2–29.

21 Y. Wu, S. Li, Y. Chen, W. He and Z. Guo, *Chem. Sci.*, 2022, **13**, 5085–5106.

22 L. C.-C. Lee and K. K.-W. Lo, *Small Methods*, 2024, **8**, 2400563.

23 A. K. Yadav, R. Kushwaha, A. A. Mandal, A. Mandal and S. Banerjee, *J. Am. Chem. Soc.*, 2025, **147**, 7161–7181.

24 Q. Zhao, C. Huang and F. Li, *Chem. Soc. Rev.*, 2011, **40**, 2508–2524.

25 E. Baggaley, J. A. Weinstein and J. A. G. Williams, *Coord. Chem. Rev.*, 2012, **256**, 1762–1785.

26 L. C.-C. Lee and K. K.-W. Lo, *Chem. Rev.*, 2024, **124**, 8825–9014.

27 C.-P. Tan, Y.-M. Zhong, L.-N. Ji and Z.-W. Mao, *Chem. Sci.*, 2021, **12**, 2357–2367.

28 L. C.-C. Lee and K. K.-W. Lo, *J. Am. Chem. Soc.*, 2022, **144**, 14420–14440.

29 L. C.-C. Lee and K. K.-W. Lo, *ACS Cent. Sci.*, 2025, **11**, 1289–1305.

30 A. A. Mandal, R. Kushwaha, A. K. Yadav and S. Banerjee, *ChemBioChem*, 2023, **24**, e202200597.

31 R. L. Siegel, T. B. Kratzer, A. N. Giaquinto, H. Sung and A. Jemal, *Ca-Cancer J. Clin.*, 2025, **75**, 10–45.

32 S. Tohme, R. L. Simmons and A. Tsung, *Cancer Res.*, 2017, **77**, 1548–1552.

33 H. E. Barker, J. T. E. Paget, A. A. Khan and K. J. Harrington, *Nat. Rev. Cancer*, 2015, **15**, 409–425.

34 C. Holohan, S. Van Schaeybroeck, D. B. Longley and P. G. Johnston, *Nat. Rev. Cancer*, 2013, **13**, 714–726.

35 C. Liang, J. Xie, S. Luo, C. Huang, Q. Zhang, H. Huang and P. Zhang, *Nat. Commun.*, 2021, **12**, 5001.

36 J. Xie, C. Liang, S. Luo, Z. Pan, Y. Lai, J. He, H. Chen, Q. Ren, H. Huang, Q. Zhang and P. Zhang, *ACS Appl. Mater. Interfaces*, 2021, **13**, 27934–27944.

37 Z. Lv, P. Zhang, K. Hua and J. Jiang, *J. Organomet. Chem.*, 2025, **1029**, 123547.

38 G. Ren, Q. Meng, P. Li, C. Wang, C. Wu, S. Zhu, Y. Li, R. Liu, C. Zhu and H. Zhu, *Inorg. Chem. Front.*, 2025, **12**, 6286–6296.

39 L. Guan, S. Tao, X. Lu, Y. Jiang, K. Xu, J. Peng, W. Shen, G. Guo, Z. Shen and J. Ru, *J. Med. Chem.*, 2025, **68**, 14008–14018.

40 Y. Lai, N. Lu, A. Ouyang, Q. Zhang and P. Zhang, *Chem. Sci.*, 2022, **13**, 9921–9926.

41 H. Wang, D. Li, H. Wang, Q. Ren, Y. Pan, A. Dao, D. Wang, Z. Wang, P. Zhang and H. Huang, *J. Med. Chem.*, 2024, **67**, 18356–18367.

42 D. Xu, Q. Dai, J. Sun, Y. An, Z. Wang, L. Yang, Z. Lu, C. Chu and G. Liu, *Ultrason. Sonochem.*, 2025, **119**, 107415.

43 S. Hernot and A. L. Klibanov, *Adv. Drug Delivery Rev.*, 2008, **60**, 1153–1166.

44 X. Qian, Y. Zheng and Y. Chen, *Adv. Mater.*, 2016, **28**, 8097–8129.

45 P. Nittayacharn, E. Abenojar, M. La Deda, L. Ricciardi, G. Strangi and A. A. Exner, *Bioconjugate Chem.*, 2022, **33**, 1057–1068.

46 M. Fan, Y. Han, S. Gao, H. Yan, L. Cao, Z. Li, X.-J. Liang and J. Zhang, *Theranostics*, 2020, **10**, 4944–4957.

47 J. Zhu, A. Ouyang, Z. Shen, Z. Pan, S. Banerjee, Q. Zhang, Y. Chen and P. Zhang, *Chin. Chem. Lett.*, 2022, **33**, 1907–1912.

48 X. Wang, X. Zhong and L. Cheng, *Coord. Chem. Rev.*, 2021, **430**, 213662.

49 G. Li, S. Wu, J. Liu, K. Wang, X. Chen and H. Liu, *Adv. Mater.*, 2024, **36**, 2401252.

50 V. G. Collins, D. Hutton, K. Hossain-Ibrahim, J. Joseph and S. Banerjee, *Br. J. Cancer*, 2025, **132**, 409–420.

51 Y. Yang, J. Huang, M. Liu, Y. Qiu, Q. Chen, T. Zhao, Z. Xiao, Y. Yang, Y. Jiang, Q. Huang and K. Ai, *Adv. Sci.*, 2023, **10**, 2204365.

52 S. Liang, J. Yao, D. Liu, L. Rao, X. Chen and Z. Wang, *Adv. Mater.*, 2023, **35**, 2211130.

53 C. Zhang and K. Pu, *Adv. Mater.*, 2023, **35**, 2303059.

54 D. V. Krysko, A. D. Garg, A. Kaczmarek, O. Krysko, P. Agostinis and P. Vandenabeele, *Nat. Rev. Cancer*, 2012, **12**, 860–875.

55 D. Tang, M. Cui, B. Wang, C. Xu, Z. Cao, J. Guo, H. Xiao and K. Shang, *Adv. Mater.*, 2024, **36**, 2406815.

56 D. S. Schwarz and M. D. Blower, *Cell. Mol. Life Sci.*, 2016, **73**, 79–94.

57 X. Xu, M. Chen, S. Jiang, Z. Pan and C. Zhao, *Adv. Funct. Mater.*, 2024, **34**, 2314780.

58 Y. Tan, Z. Wang, Y. An, M. Li, D. Xu, R. Liu, X. Tan, Y. He, Z. Lu and G. Liu, *Chin. Chem. Lett.*, 2026, **37**, 111214.

59 X. Wu, J.-J. Hu and J. Yoon, *Angew. Chem., Int. Ed.*, 2024, **63**, e202400249.

60 X. Xu, J. Zheng, N. Liang, X. Zhang, S. Shabiti, Z. Wang, S. Yu, Z.-Y. Pan, W. Li and L. Cai, *ACS Nano*, 2024, **18**, 9413–9430.

61 X. Xu, S. Shabiti, X. Zhang, J. Zheng, N. Liang, Z. Wang, S. Yu, Y. Wang, S. Jiang, Z. Pan, W. Li and L. Cai, *Nano Today*, 2024, **56**, 102270.

62 A. L. Harris, *Nat. Rev. Cancer*, 2002, **2**, 38–47.

63 X. Jiang, J. Wang, X. Deng, F. Xiong, J. Ge, B. Xiang, X. Wu, J. Ma, M. Zhou, X. Li, Y. Li, G. Li, W. Xiong, C. Guo and Z. Zeng, *Mol. Cancer*, 2019, **18**, 10.

64 C. Li, Y. Gao, Y. Wang, J. Wang, J. Lin, J. Du, Z. Zhou, X. Liu, S. Yang and H. Yang, *Adv. Funct. Mater.*, 2023, **33**, 2210348.

65 X. Li, H. Qian, J. Du, J. Pan, Q. Wang, H. Yang, L. Gu, X. Zhang, Y. Miao and Y. Li, *Chem. Eng. J.*, 2025, **507**, 160713.

66 X. Wu, J. Liang, J. Shu, Z. Li, T. Yin, X. Zhang and H. Chao, *J. Am. Chem. Soc.*, 2025, **147**, 15329–15343.

67 L. Chen, J. Min and F. Wang, *Signal Transduction Targeted Ther.*, 2022, **7**, 378.

68 W.-Q. Liu, W.-R. Lin, L. Yan, W.-H. Xu and J. Yang, *Immunol. Rev.*, 2024, **321**, 211–227.

69 J. Huang, F. Hu, H. Zhang, Z. Cao, H. Xiao, Z. Yang, Q. Jin and K. Shang, *Adv. Mater.*, 2025, **37**, 2504228.

70 R. B. Mokhtari, T. S. Homayouni, N. Baluch, E. Morgatskaya, S. Kumar, B. Das and H. Yeger, *Oncotarget*, 2017, **8**, 38022–38043.

71 S. Son, J. H. Kim, X. Wang, C. Zhang, S. A. Yoon, J. Shin, A. Sharma, M. H. Lee, L. Cheng, J. Wu and J. S. Kim, *Chem. Soc. Rev.*, 2020, **49**, 3244–3261.

72 S. Liang, X. Deng, P. Ma, Z. Cheng and J. Lin, *Adv. Mater.*, 2020, **32**, 2003214.

73 M. Xu, L. Zhou, L. Zheng, Q. Zhou, K. Liu, Y. Mao and S. Song, *Cancer Lett.*, 2021, **497**, 229–242.

74 C. Szabo, *Nat. Rev. Drug Discovery*, 2016, **15**, 185–203.

75 R. Motterlini and L. E. Otterbein, *Nat. Rev. Drug Discovery*, 2010, **9**, 728–743.

76 K. Ling, F. Men, W.-C. Wang, Y.-Q. Zhou, H.-W. Zhang and D.-W. Ye, *J. Med. Chem.*, 2018, **61**, 2611–2635.

77 L. C.-C. Lee, K.-K. Leung and K. K.-W. Lo, *Dalton Trans.*, 2017, **46**, 16357–16380.

78 J. Zhu, A. Ouyang, J. He, J. Xie, S. Banerjee, Q. Zhang and P. Zhang, *Chem. Commun.*, 2022, **58**, 3314–3317.

79 R. Kushwaha, V. Singh, S. Peters, A. K. Yadav, T. Sadhukhan, B. Koch and S. Banerjee, *J. Med. Chem.*, 2024, **67**, 6537–6548.

80 Y. Li, N. Lu, Q. Lin, H. Wang, Z. Liang, Y. Lu and P. Zhang, *Chin. Chem. Lett.*, 2023, **34**, 107653.

81 A. K. Yadav, V. Singh, S. Acharjee, S. Saha, R. Kushwaha, A. Dutta, B. Koch and S. Banerjee, *Chem.–Eur. J.*, 2024, **31**, e202403454.

82 G. Liang, T. Sadhukhan, S. Banerjee, D. Tang, H. Zhang, M. Cui, N. Montesdeoca, J. Karges and H. Xiao, *Angew. Chem., Int. Ed.*, 2023, **62**, e202301074.

83 G. Liu, Y. Zhang, H. Yao, Z. Deng, S. Chen, Y. Wang, W. Peng, G. Sun, M.-K. Tse, X. Chen, J. Yue, Y.-K. Peng, L. Wang and G. Zhu, *Sci. Adv.*, 2023, **9**, eadg5964.

84 C. Kong, Y. Li, Y. Xu, C. Luo, N. Shen, Z. Tang and X. Chen, *CCS Chem.*, 2025, **7**, 1142–1156.

85 M. Shen, Y. Wang, L. Zhang, T. Bing, X. Li, L. Zhu, S. Wen, G. Chen and Y. Yu, *Adv. Funct. Mater.*, 2025, **35**, 2425565.

86 M. He, Z. Ma, L. Zhang, Z. Zhao, Z. Zhang, W. Liu, R. Wang, J. Fan, X. Peng and W. Sun, *J. Am. Chem. Soc.*, 2024, **146**, 25764–25779.

87 Y. Zheng, J. Ye, Z. Li, H. Chen and Y. Gao, *Acta Pharm. Sin. B*, 2021, **11**, 2197–2219.

88 Z. Chen, T. Feng, J. Shen, J. Karges, C. Jin, Y. Zhao, L. Ji and H. Chao, *Inorg. Chem. Front.*, 2022, **9**, 3034–3046.

89 D.-D. Xie, X.-L. Li, L.-Z. Zeng, X. Ren, D. Zhang, R. Yang and F. Gao, *ChemBioChem*, 2025, **26**, e202400801.

90 X. Li, J. F. Lovell, J. Yoon and X. Chen, *Nat. Rev. Clin. Oncol.*, 2020, **17**, 657–674.

91 J. Shen, J. Karges, K. Xiong, Y. Chen, L. Ji and H. Chao, *Biomaterials*, 2021, **275**, 120979.

92 X.-X. Ren, X.-L. Li, R.-Y. Zhao, Y. Li, R. Song, M.-C. Han, Y.-F. Yan, L.-Z. Zeng, Z.-Y. Cai and F. Gao, *Inorg. Chem.*, 2025, **64**, 9596–9607.

93 R. Song, R.-Y. Zhao, R. Yan, X.-L. Li, L.-Z. Zeng, Z. Cai, J. Chen, X. Ren, X. Cheng and F. Gao, *J. Med. Chem.*, 2025, **68**, 17653–17666.

94 C. J. L. Murray, K. S. Ikuta, F. Sharara, L. Swetschinski, G. R. Aguilar, A. Gray, C. Han, C. Bisignano, P. Rao, E. Wool, S. C. Johnson, A. J. Browne, M. G. Chipeta, F. Fell, S. Hackett, G. Haines-Woodhouse, B. H. K. Hamadani, E. A. P. Kumaran, B. McManigal, S. Achalapong, R. Agarwal, S. Akech, S. Albertson, J. Amuasi, J. Andrews, A. Aravkin, E. Ashley, F.-X. Babin, F. Bailey, S. Baker, B. Basnyat, A. Bekker, R. Bender, J. A. Berkley, A. Bethou, J. Bielicki, S. Boonkasidecha, J. Bukosia, C. Carvalheiro, C. Castañeda-Orjuela, V. Chansamouth, S. Chaurasia, S. Chiurchiù, F. Chowdhury, R. C. Donatien, A. J. Cook, B. Cooper, T. R. Cressey, E. Criollo-Mora, M. Cunningham, S. Darboe, N. P. J. Day, M. De Luca, K. Dokova, A. Dramowski, S. J. Dunachie, T. D. Bich, T. Eckmanns, D. Eibach, A. Emami, N. Feasey, N. Fisher-Pearson, K. Forrest, C. Garcia, D. Garrett, P. Gastmeier, A. Z. Giref, R. C. Greer, V. Gupta, S. Haller, A. Haselbeck, S. I. Hay, M. Holm, S. Hopkins, Y. Hsia, K. C. Iregbu, J. Jacobs, D. Jarovsky, F. Javanmardi, A. W. J. Jenney, M. Khorana, N. Kissoon, E. Kobeissi, T. Kostyanev, K. Phommasone, S. Khusuwan, F. Krapp, R. Krumkamp, A. Kumar, H. H. Kyu, C. Lim, K. Lim, D. Limmathurotsakul, M. J. Loftus, M. Lunn, J. Ma, A. Manoharan, F. Marks, J. May, M. Mayxay, N. Mturi, T. Munera-Huertas, P. Musicha, L. A. Musila, M. M. Mussi-Pinhata, R. N. Naidu, T. Nakamura, R. Nanavati, S. Nangia, P. Newton, C. Ngoun, A. Novotney, D. Nwakanma, C. W. Obiero, T. J. Ochoa, A. Olivas-Martinez, P. Olliaro, E. Ooko, E. Ortiz-Brizuela, P. Ounchanum, G. D. Pak, J. L. Paredes, A. Y. Peleg, C. Perrone, T. Phe, N. Plakkal, A. Ponce-de-Leon, M. Raad, T. Ramdin, S. Rattanavong, A. Riddell, T. Roberts, J. V. Robotham, A. Roca, V. D. Rosenthal, K. E. Rudd, N. Russell, H. S. Sader, W. Saengchan, J. Schnall, J. A. G. Scott, S. Seekaew, M. Sharland, M. Shivamallappa, J. Sifuentes-Osornio, A. J. S. N. Steenkeste, A. J. Stewardson, T. Stoeva, N. Tasak, A. Thaiprakong, G. Thwaites, C. Tigoi, C. Turner, P. Turner, H. R. van Doorn, S. Velaphi, A. Vongpradith, M. Vongsouvath, H. Vu, T. Walsh, J. L. Walson, S. Waner, T. Wangrangsimakul, P. Wannapinij, T. Wozniak, T. E. M. W. Young-Sharma, K. C. Yu, P. Zheng, B. Sartorius, A. D. Lopez, A. Stergachis, C. Moore, C. Dolecek and M. Naghavi, *Lancet*, 2022, **399**, 629–655.

95 L. Hall-Stoodley, J. W. Costerton and P. Stoodley, *Nat. Rev. Microbiol.*, 2004, **2**, 95–108.

96 Y. Li, H. Wang, Q. Lin, X. Yu, H. Huang and P. Zhang, *Sci. China: Chem.*, 2023, **66**, 2645–2653.

97 Y. Xu, Y. Pang, L. Luo, A. Sharma, J. Yang, C. Li, S. Liu, J. Zhan and Y. Sun, *Angew. Chem., Int. Ed.*, 2024, **63**, e202319966.

98 Y. Wang, L. Luo, T. Zhang, J.-R. Hu, H. Wang, F. Bao, C. Li, Y. Sun and J. Li, *ACS Appl. Mater. Interfaces*, 2024, **16**, 52068–52079.

99 Q. Li, Y. Pang, L. Mei, S. Liang, H. Wang, Y. Jiao, S. Qiu, H. Chen, X. Xing and Y. Sun, *Inorg. Chem. Front.*, 2025, **12**, 2668–2677.

100 S. S. Martin, A. W. Aday, N. B. Allen, Z. I. Almarzooq, C. A. M. Anderson, P. Arora, C. L. Avery, C. M. Baker-Smith, N. Bansal, A. Z. Beaton, Y. Commodore-Mensah, M. E. Currie, M. S. V. Elkind, W. Fan, G. Generoso, B. B. Gibbs, D. G. Heard, S. Hiremath, M. C. Johansen, D. S. Kazi, D. Ko, M. H. Leppert, J. W. Magnani, E. D. Michos, M. E. Mussolino, N. I. Parikh, S. M. Perman, M. Rezk-Hanna, G. A. Roth, N. S. Shah, M. V. Springer, M.-P. St-Onge, E. L. Thacker, S. M. Urbut, H. G. C. Van Spall, J. H. Voeks, S. P. Whelton, N. D. Wong, S. S. Wong, K. Yaffe and L. P. Palaniappan, *Circulation*, 2025, **151**, e41–e660.

101 N. Mackman, W. Bergmeier, G. A. Stouffer and J. I. Weitz, *Nat. Rev. Drug Discovery*, 2020, **19**, 333–352.

102 K. Stark and S. Massberg, *Nat. Rev. Cardiol.*, 2021, **18**, 666–682.

103 Z. Wu, L. Zhang, Z. Wang, S. Liu, Q. Zhang, C. Shi, Y. Wang, G. Xu, D. Zhu, M. R. Bryce, L. Ren and B. Z. Tang, *Adv. Mater.*, 2025, **37**, 2503599.

104 Y. Pang, Q. Li, J. Wang, S. Wang, A. Sharma, Y. Xu, H. Hu, J. Li, S. Liu and Y. Sun, *Angew. Chem., Int. Ed.*, 2025, **64**, e202415802.

105 C. Xu, J. Huang, Y. Jiang, S. He, C. Zhang and K. Pu, *Nat. Biomed. Eng.*, 2023, **7**, 298–312.